# Intestinal LKB1 loss drives a pre-malignant program along the serrated cancer pathway

Plugge S.F.[#,1], Ma H.[#,1,2], van der Vaart J.Y.[1], Sprangers J.[1], Morsink F.H.M.[2], Xanthakis D.[1], Jamieson C.[1], Keijzer A.R.[1], Margaritis T[3]., Candelli T.[3], Straver R.[1], de Ridder J.[1], Holstege F.C.P.[3, 4], de Leng W.W.J.[2], Offerhaus G.J.A.[2], Merenda A.*[,1], Maurice M.M.*,[1]

1. Center for Molecular Medicine and Oncode Institute, University Medical Center Utrecht, Utrecht, The Netherlands
2. Department of Pathology, University Medical Center Utrecht, Utrecht, The Netherlands
3. Princess Maxima Center for Pediatric Oncology, Utrecht, Utrecht, The Netherlands
4. Center for Molecular Medicine, University Medical Center Utrecht, Utrecht, The Netherlands

[#]These authors contributed equally

*Corresponding authors

## Abstract

Peutz-Jeghers syndrome (PJS) is a familial disorder caused by heterozygous inactivating Liver Kinase B1 (*LKB1/STK11)* mutations that induce hamartomatous polyp formation in the gastrointestinal tract. Additionally, PJS patients carry an elevated risk of developing malignancies in multiple tissues, including the intestine. How *LKB1* deficiency alters the hierarchical organization and phenotypical landscape of epithelial tissues to mediate an increased cancer risk remains poorly understood. Here, we investigate these issues using small intestinal organoids that carry heterozygous or homozygous *Lkb1* mutations. We show that *Lkb1* loss causes allele dosage-dependent activation of transcriptional programs for tissue repair, particularly within stem and transit amplifying cell lineages. Furthermore, enhanced EGFR ligand expression promotes niche-independent growth of *Lkb1*-deficient organoids. Strikingly, we uncover that mono-allelic loss of *Lkb1* is sufficient to shift the epithelium into the serrated premalignant program for colorectal carcinogenesis, which is strongly amplified upon loss-of-heterozygosity (LOH) or activating *Kras* mutations. We conclude that heterozygous mutations in LKB1 predispose the intestinal epithelium to uncontrolled growth along the serrated pathway, providing an explanation for the increased cancer risk in PJS patients.

## Introduction

The Peutz-Jeghers syndrome (PJS) is a hereditary genetic disorder that occurs in approximately 1:50.000 - 1:200.000 individuals worldwide (Beggs *et al.*, 2010). PJS patients suffer from a life-long development of benign hamartomatous polyps throughout their gastrointestinal tract for which they need periodical surgical resection. Moreover, patients carry an increased risk of developing early-onset epithelial tumors, particularly within the gastrointestinal (GI) tract (up to 66%), breast (up to 54%), pancreas (up to 36%) and gonads (Giardiello *et al.*, 2000; Hearle *et al.*, 2006; Beggs *et al.*, 2010; Van Lier *et al.*, 2010), resulting in a cumulative lifetime risk of 93% (Giardiello *et al.*, 2000). Of note, PJS patients are predisposed to malignancies of the small intestine (frequency 13%), a condition that is otherwise very rare (0.03%) (Van Lier *et al.*, 2010; Tomasetti and Vogelstein, 2015).

Heterozygous inactivating mutations in the tumor suppressor gene Liver Kinase B1 (*LKB1/STK11*) were identified as the main cause of PJS (Hemminki *et al.*, 1998; Jenne *et al.*, 1998). Furthermore, *LKB1* mutations are causally linked to a broad range of sporadic cancer cases, including lung carcinoma, melanoma, pancreatic and cervical cancers (Giardiello and Trimbath, 2006; Sanchez-Cespedes, 2007). *LKB1* encodes a serine/threonine kinase implicated in the regulation of a variety of critical cellular processes, including energy metabolism, cell adhesion, DNA methylation and apicobasal polarity (Shackelford and Shaw, 2009; Kline *et al.*, 2013; Pierce *et al.*, 2021). Loss of heterozygosity (LOH) in this gene is regarded as a driving force of cancer development, as over 64% of PJS-derived carcinomas present with inactivation of the second copy of the gene (Entius *et al.*, 2001; De Leng *et al.*, 2003).

Over recent years, modelling of PJS in murine models revealed that *Lkb1* loss in either mesenchymal or T cell lineages induces development of gastro-intestinal polyps with strong resemblance to those observed in PJS patients. (Katajisto *et al.*, 2008; Ollila *et al.*, 2018; Poffenberger *et al.*, 2018; Cotton *et al.*, 2022). These results have shifted focus to non-epithelial roles of *Lkb1* in driving PJS disease development, with an emphasis on processes underlying polyposis. If and how polyp formation in PJS patients links to cancer predisposition however remains a heavily debated issue, as LOH and dysplastic transformation of PJS polyps were reported to be very rare (Shepherd, Bussey and Jass, 1987; Entius *et al.*, 2001; De Leng *et al.*, 2003; Korsse *et al.*, 2013). These observations differ from other polyposis syndromes, such as familial adenomatous polyposis (FAP), where epithelial loss of the underlying germline mutation in the adenomatous polyposis coli gene APC and its role in cancer development has been well described (Fodde, 2002).

Since *LKB1* loss mediates predisposition to carcinoma development in multiple epithelial tissues irrespective of polyp formation, we hypothesized that epithelial-intrinsic alterations may sensitize these tissues to cancer formation. Previous studies indicate that intestinal epithelial loss of *LKB1* does not lead to polyp formation while alterations in secretory cell fate specification were identified (Shorning *et al.*, 2009; Gao *et al.*, 2020; Cotton *et al.*, 2022; Kim *et al.*, 2022). Despite these advancements, how epithelial *LKB1* loss changes the phenotypic landscape of the intestinal epithelium and how these alterations may link to cancer predisposition in PJS patients remains poorly understood.

Here, we model *mono-* and *bi*-allelic inactivation of *Lkb1* in small intestinal organoids to investigate how *Lkb1* loss alters the dynamics of cellular identities and lineage relationships of the intestinal epithelium. We uncover that *Lkb1* loss promotes features of epithelial transformation linked to the serrated pathway for intestinal carcinogenesis. These features include loss of classical adult stem cell populations, activation of transcriptional programs related to regeneration and intestinal-to-gastric cellular transdifferentation, as well as the acquirement of niche-independent growth properties. Our findings argue that *Lkb1* loss mediates epithelium-wide activation of a pre-cancer program akin to sporadic serrated precursor lesions, providing an explanation for the increased cancer risk observed in PJS patients. By linking *Lkb1* loss to a major pathway for colorectal cancer development, these findings pave a path for the development of new strategies for prevention, surveillance and precision treatment of PJS tumors as well as other malignancies harboring *LKB1* inactivating mutations.

## Results

### *Lkb1* bi-allelic loss results in phenotypic heterogeneity and increased self-renewal potential of small intestinal organoids.

To study the role of *Lkb1* loss in the intestinal epithelium, we employed CRISPR/Cas9 technology to generate *Lkb1*-deficient mouse small intestinal organoid lines. To obtain homogenous organoid cultures that are either heterozygous or homozygous for *Lkb1* loss, we isolated single organoids from bulk cultures and expanded these as individual clones. After genotyping, we selected one *Lkb1*$^{+/-}$ and two *Lkb1*$^{-/-}$ clonal lines for further characterization (Figure S1A, Figure 1A-B). *Lkb1*$^{+/-}$ organoids were morphologically similar to wild type (WT) organoids, with typical budding structures that reflect a crypt-villus organization (Sato *et al.*, 2009) (Figure 1A). Remarkably, the introduction of homozygous *Lkb1* loss resulted in phenotypic bifurcation, with clonal lines displaying either a budding or a cystic growth morphology (Figure 1A). Notably, from day 3 after passaging, budding *Lkb1*$^{-/-}$ (*Lkb1*$^{bud\ -/-}$) organoids accumulated clusters of dead cells in their periphery (Figure 1A), as indicated by their positive staining for cleaved caspase 3 (Figure S1B). These observations are different from *Lkb1*$^{+/-}$ and WT organoids that mainly accumulate dead cells in their lumen (Figure S1B) (Sato *et al.*, 2009).

Next, we tested whether *Lkb1* loss alters the ability of intestinal organoids to reconstitute organoids from single cells, as a proxy for their self-renewal capacity. While budding WT and *Lkb1*-mutant organoids lines displayed similar outgrowth rates, cystic *Lkb1*$^{-/-}$ (*Lkb1*$^{cys\ -/-}$) organoids carried a significantly improved capacity to form organoids upon seeding of single cells (Figure 1C). Regardless of these observations, both homozygous mutant morphologies displayed a similar increase in the number of proliferative cells in comparison to heterozygous and wild-type organoids, as shown by EdU incorporation (Figure 1D, E). To rule out that changes in organoid morphology of the homozygous mutants are the result of CRISPR off-target effects, we used an alternative gRNA to introduce *Lkb1* mutations, which resulted in an identical phenotypic heterogeneity of *Lkb1*$^{-/-}$ organoid lines (Figure S1C-E). Moreover, these newly generated *Lkb1*$^{cys\ -/-}$ clones also displayed superior reconstitution potential compared to their homozygous budding counterparts (Figure S1F). These findings reveal that biallelic *Lkb1* loss results in phenotypic heterogeneity within the intestinal epithelium, and that homozygous *Lkb1*-mutant organoids with cystic morphology display an increased recovery potential.

### *Lkb1* loss alters the number, morphology and positioning of secretory cells.

To investigate whether our *Lkb1*-mutant organoid lines serve as representative models for intestinal epithelial loss of *Lkb1 in vivo*, we examined alterations in localization and morphology of Paneth (Lyz$^{+}$) and goblet (Muc2$^{+}$) cells that were previously reported for the *Lkb1*-mutant mouse intestine (Shorning *et al.*, 2009; Gao *et al.*, 2020). Compared to WT organoids, the localization of Lyz1$^{+}$ cells in *Lkb1*$^{+/-}$ and *Lkb1*$^{bud\ -/-}$ organoids was not restricted to the bottom of the crypt but displayed a more scattered distribution that reached into the villus domain (Figure 2A). In addition, while Muc2$^{+}$ cells in WT and *Lkb1*$^{+/-}$ organoids were present in modest numbers and always located to the villus region, Muc2$^{+}$ cell numbers were increased in *Lkb1*$^{bud\ -/-}$ organoids and found scattered throughout the crypt-villus axis (Figure 2B). These observations are highly reminiscent of the reported aberrancies in Paneth and Goblet cell numbers and localization in the *Lkb1*-deficient mouse intestine *in vivo* (Shorning *et al.*, 2009). By contrast, *Lkb1*$^{cys\ -/-}$ organoids were devoid

of Lyz1$^{+}$ cells but did allow for formation of Muc2$^{+}$ cells that are usually lacking in cystic organoids (Sato, Es, *et al.*, 2011), indicating that secretory lineage specification is also altered within these organoids (Figure 2A-B).

We next investigated how these findings relate to intestinal tissue organization of human PJS patients. While the average number and location of MUC2$^{+}$ cells per intestinal crypt was similar for healthy donors and the non-transformed epithelium of PJS patients (Figure 2C, Figure S2A-B), LYZ1$^{+}$ cells were clearly mislocalized within the PJS mucosa (Figure 2D). In the healthy intestine, LYZ1$^{+}$cells localized strictly to the crypt base in the healthy intestine, as expected (Barker *et al.*, 2007). In the non-transformed epithelium of PJS patients, however, LYZ1$^{+}$ cells frequently scattered towards higher regions of the crypt (Figure 2D). Thus, heterozygous loss of *LKB1* in PJS patient-derived intestines leads to mislocalization of LYZ1$^{+}$cells but does not alter MUC2$^{+}$ cell distribution, similar to our observations in *Lkb1*$^{+/-}$ organoids.

To examine *Lkb1* loss-induced alterations in secretory cell morphology at the ultrastructural level, we employed electron microscopy. In WT intestinal organoids, Paneth cells displayed a typical morphology with prominent apical accumulation of spherically-shaped secretory granules that are uniformly filled with electron-dense content (Figure 2E) (Satoh *et al.*, 1990; Sato *et al.*, 2009). By contrast, secretory granules of *Lkb1*$^{+/-}$ Paneth cells commonly contained an abnormally 'sausage-shaped' electron-dense core (Figure 2E). In *Lkb1*$^{bud-/-}$ organoids, the content of Paneth cell-secretory granules was even more aberrant, displaying a small electron-dense core surrounded by a peripheral electron-lucent halo (Figure 2E). In WT intestinal organoids, columnar-shaped goblet cells were identified with large translucent granules filled with mucus (Figure 2F) (Troughton and Trier, 1969; Bansil and Turner, 2018). Compared to WT goblet cells, *Lkb1*$^{+/-}$ mucus-secreting cells displayed a rounded and more flattened morphology while *Lkb1*$^{bud\ -/-}$ goblet-like cells display granules with an unusual electron dense core (Figure 2F). In addition, in *Lkb1*$^{cys-/-}$ organoids the content of these mucus-like granules was frequently lost during EM preparation, suggesting an altered mucin composition, which might also explain the limited number of identified Muc2$^{+}$ cells (Figure 2F). The morphology of these Paneth-like and goblet-like cells in *Lkb1*-deficient organoids is reminiscent of a previously described population of 'intermediate' cells that were proposed to represent transition states between undifferentiated and more mature secretory cells (Troughton and Trier, 1969). Together, these observations suggest that *Lkb1* loss may interfere with the terminal differentiation of secretory cells. Furthermore, previous studies identified roles of *LKB1* in apical brush border formation, using 2D human (cancer) cell lines (Baas *et al.*, 2004). Inspection of our EM images however did not reveal any evidence for loss of these subcellular structures in *Lkb1*-deficient organoids (Figure S2C).

Taken together, our findings reveal that engineering *Lkb1* loss in organoids induces highly similar alterations in secretory cell number, localization and morphology as those observed in *in vivo* mouse models and the intestine of PJS patients. These results thus confirm the suitability and relevance of organoids for modelling epithelial alterations in PJS. Furthermore, our results indicate that *Lkb1* loss-induced alterations in cell lineage specification and positioning are intrinsic to the epithelium and do not rely on interactions with the mesenchyme.

***Lkb1* mono- and bi-allelic loss induces incremental expression of a regenerative gene signature.**

To examine how *Lkb1* loss affects epithelial organization, we determined transcriptional changes induced by *Lkb1* loss in organoids using bulk mRNA sequencing. Compared to WT organoids, we observed differential

expression of 1298, 2312 and 7816 genes in *Lkb1*$^{+/-}$, *Lkb1*$^{bud\ -/-}$ and *Lkb1*$^{cys\ -/-}$ organoids, respectively (Supplementary Table 1). Using gene set enrichment analysis (GSEA) we first examined the consequences of *Lkb1* loss on well-defined gene signatures derived from individual intestinal cell types (Haber *et al.*, 2017). In agreement with our earlier results, all *Lkb1*-deficient clones showed significant downregulation of gene sets linked to mature Paneth cells, whereas goblet cell gene sets were enriched within both budding and cystic *Lkb1*$^{-/-}$ organoids in comparison to WT organoids, again suggesting alterations in secretory cell lineage specification (Figure 3A).

Noticeably, the *Lgr5*$^{+}$ adult stem cell signature (Haber *et al.*, 2017) was downregulated in all *Lkb1*-deficient clones (Figure 3A). These data are reminiscent of the previously reported growth state of fetal intestinal spheroids that relies on proliferation of *Lgr5*-negative progenitors (Mustata *et al.*, 2013). Indeed, we uncovered a gradual enrichment of an embryonic spheroid gene signature in *Lkb1*-deficient organoids (Mustata *et al.*, 2013), that correlated with the number of lost *Lkb1* alleles (Figure 3A-B). The transition from adult stem cell to a fetal spheroid signature was most striking for *Lkb1*$^{cys\ -/-}$ organoids compared to *Lkb1*$^{bud\ -/-}$ organoids (Figure 3B). Previous studies indicated that a transient upregulation of a fetal-like intestinal gene signature associates with epithelial remodeling during injury repair and wound healing (Fordham *et al.*, 2013; Nusse *et al.*, 2018; Yui, Azzolin, Maimets, Pedersen, Fordham, Hansen, Larsen, Guiu, M. R. P. Alves, *et al.*, 2018; Wang *et al.*, 2019). In line with these observations, *Lkb1*-deficient organoid clones also exhibited enrichment of gene signatures associated with intestinal regeneration response following damage or infection (Figure 3A). To rule out that organoid morphology rather than *Lkb1*-deficiency mediates expression of this regenerative program, we analyzed the transcriptomes of *Apc*$^{-/-}$ and Wnt-treated organoids that also exhibit a cystic shape but are WT for *Lkb1* (Merenda, Fenderico and Maurice, 2020). In comparison to both *Apc*$^{-/-}$ and Wnt-treated organoids, *Lkb1*$^{cys\ -/-}$ organoids were significantly enriched for expression of these regenerative gene sets, confirming that *Lkb1* loss itself promotes a regenerative state (Figure S3A). Furthermore, *Lkb1*-deficient clones, as well as control fetal intestinal organoids (E16.5), displayed increased expression of the fetal marker Anxa1, while this marker was not detected in WT adult intestinal organoids (Figure 3C) (Yui, Azzolin, Maimets, Pedersen, Fordham, Hansen, Larsen, Guiu, M. R. P. Alves, *et al.*, 2018). In addition, a dysplastic region of human PJS patient-derived duodenal epithelial tissue showed patches of ANXA1-positive epithelial cells, while non-transformed PJS and healthy donor duodenum epithelial cells remained negative (Figure 3D). Together, these findings indicate that *Lkb1* loss converts the epithelium into a permanent regenerative state. Strikingly, this conversion towards a tissue repair growth state is already apparent upon monoallelic *Lkb1* loss, a representative condition for the PJS intestinal epithelium.

**_Lkb1_-deficient organoids show a Yap-induced regenerative state and display intra-epithelial self-sufficiency for Egf.**

Over recent years, Yap signaling was placed central to intestinal regeneration (Gregorieff *et al.*, 2015). Additionally, *LKB1* was uncovered previously as a negatively regulator of the Hippo-Yap pathway in an siRNA kinome screen (Mohseni *et al.*, 2014). We therefore wondered if *Lkb1* loss may activate Yap signaling as part of the induced regenerative program in intestinal epithelial organoids. Indeed, we identified enhanced expression of a Yap-regulated gene signature linked to intestinal regeneration (Gregorieff *et al.*, 2015) in *Lkb1*-mutant organoids (Figure 3A). Notably, increased Yap target gene expression was already identified in heterozygous *Lkb1*-mutant conditions and progressively increased with loss of both *Lkb1* alleles (Figure

S3B). Again, *Lkb1*$^{cys\ -/-}$ organoids showed the strongest induction of Yap target genes, in line with their robust expression of a regenerative transcriptional program (Figure S3B). Immunofluorescence staining further confirmed an increase in Yap protein expression in both budding and cystic *Lkb1*$^{-/-}$ organoids, and a prominent nuclear localization of Yap, particularly within *Lkb1*$^{cys\ -/-}$ organoids (Figure 4A-B).

YAP pathway activation is well-known to induce enhanced expression of EGF family ligands, particularly in the context of regeneration (Zhang *et al.*, 2009; Ren *et al.*, 2010; Yang *et al.*, 2012; Gregorieff *et al.*, 2015). We therefore wondered whether *Lkb1*-deficient organoids display altered state of EGF pathway dependency. Noticeably, we found that a combined set of the *Egf* ligand family was upregulated in *Lkb1*-deficient organoids, in a gradual manner along with *Lkb1* allelic loss and alterations in organoid morphology (Figure 5A). Furthermore, these changes were accompanied with an elevated expression of *Egf* receptor family members (Figure 5B). As survival and growth of healthy homeostatic adult intestinal organoids depends on supplementation with Egf, we investigated whether the enhanced expression of *Egf* family ligands and its receptors in *Lkb1*-deficient organoids mediates niche factor self-sufficiency, by omitting Egf from the culture medium. In contrast to WT organoids, all *Lkb1*-deficient organoids were capable of growing without Egf supplementation (Figure 5C). In support of these findings, we confirmed that organoid survival still depended on EGFR signaling, since *Lkb1*-deficient organoids were sensitive to Gefitinib, a potent EGFR inhibitor (Figure 5D).

Together, these results demonstrate that *Lkb1* loss induces a constitutive Yap-induced regenerative state and drives epithelial self-sufficiency for EGF ligand production. As niche-independent growth properties are considered a hallmark of cancer progression (Fujii *et al.*, 2016), these results provide a potential explanation for a growth advantage of *Lkb1*-deficient epithelial cells and the initiation of tumorigenesis.

**_Lkb1_-deficiency mediates reprogramming of intestinal stem cells into a regenerative state.**

To perform an in-depth analysis of how *Lkb1* loss alters intestinal lineage specification and cellular hierarchies, we subjected WT and *Lkb1*-deficient organoids to single cell RNA sequencing. We included an analysis of mouse fetal intestinal organoids, to explore a potential overlap with fetal gene expression. Unsupervised clustering of single cells identified 19 distinct clusters (Figure S4A). A clear separation of cellular profiles derived from *Lkb1*$^{cys\ -/-}$ organoids, fetal and WT cells was observed, while *Lkb1*$^{bud\ -/-}$ and *Lkb1*$^{+/-}$ organoids displayed closer resemblance to WT cells (Figure 6A). The separation of *Lkb1*$^{cys\ -/-}$ and fetal cell clusters in UMAP indicates that *Lkb1*$^{cys\ -/-}$ organoids do not fully convert to a fetal state but only show partial expression of a fetal-like gene program (Figure 6A). Furthermore, *Lkb1*$^{cys\ -/-}$ organoids are composed of a rather homogenous population of cells that are different from all budding organoid clusters and do not display a known intestinal cellular identity. We therefore restricted annotation of intestinal cell types to budding organoid lines, using publicly available intestinal cell type gene signatures (Figure 6C, Figure S4B-I) (Haber *et al.*, 2017). As the gene signatures for Paneth and goblet cells mapped to the same cluster (Figure S4E, S4H), we marked this cluster as secretory progenitors, similar to previous reports (He *et al.*, 2022). Cell type fraction analysis revealed that *Lkb1*$^{bud\ -/-}$ organoids comprise an increased fraction of secretory progenitor cells compared to WT organoids, confirming alterations in secretory cell differentiation (Figure 6B). Interestingly, the increase in secretory progenitors was accompanied with a decrease in enterocytes, suggesting that the preferred differentiation trajectory in *Lkb1*-deficient budding organoids is shifted from absorptive towards secretory lineages (Figure 6C). The previously observed morphological aberrancies in

secretory lineage specification were confirmed at the transcriptional level, as *Lkb1*-deficient organoids displayed the occurrence of 'intermediate' cells that co-express features of both Paneth and goblet cells (Figure 6D). Moreover, expression of Egf ligands was specifically increased in *Lkb1*-deficient enteroendocrine and secretory progenitor cell populations (Figure 6E) suggesting that these cells might be responsible for the observed niche-independency of *Lkb1*-mutant organoids.

As expected, expression of the fetal and regenerative marker *Anxa1* is highly abundant in both fetal and *Lkb1*$^{cys\ -/-}$ organoids (Figure 6F). Notably, we found that *Anxa1* expression in *Lkb1*$^{bud\ -/-}$ organoids is induced mainly within stem and transit amplifying (stem/TA) cell clusters, indicating that this population is the main contributor to the observed epithelial conversion into a regenerative state (Figure 6A, F). To further test this assumption, we performed reclustering of stem/TA cell populations including all *Lkb1*$^{cys\ -/-}$ cells. Unsupervised clustering indicates distinct clusters for WT, *Lkb1*$^{+/-}$ and *Lkb1*$^{bud\ -/-}$ stem/TA cells (Figure S4J-K). To examine the effect of *Lkb1* loss on intestinal stem cells, we performed GSEA on genes differentially expressed between WT stem cells and *Lkb1*-deficient stem cells (Supplementary Table 2). We observed enrichment of goblet cell gene expression within *Lkb1*-deficient stem cell populations compared to WT organoids (Figure 6G-H). This suggests that the capacity for preferential differentiation towards secretory cells is already present in *Lkb1*-deficient stem cells. Furthermore, we identified an enrichment of four out of six previously reported fetal and regenerative gene signatures, a depletion of the *Lgr5*$^{+}$ stem cell signature and an increased expression of Anxa1 in *Lkb1*-deficient stem cells (Figure 6G, I). These findings strengthen a model in which induction of a regenerative response by *Lkb1* loss originates from the stem cell compartment of the intestinal epithelium.

In conclusion, our results argue that *Lkb1*-deficient stem/TA cells reside in a regenerative state and preferentially differentiate towards secretory rather than absorptive cell lineages. As a result, secretory cells start secreting EGF ligands to drive niche-independent growth of *Lkb1*-deficient epithelium.

**_Lkb1_ loss drives a pre-malignant program along the serrated pathway which is amplified by additional _Kras_ mutations.**

Next, we aimed to obtain insight in how transcriptional reprogramming induced by *Lkb1* loss may promote cancer predisposition. Colorectal cancer (CRC) develops mainly via two pathways that involve distinct originating lesions and mutational events (Chen *et al.*, 2021). The classical adenoma-carcinoma sequence is initiated by bi-allelic mutations in the tumor suppressor APC which drives formation of stem cell-enriched adenomatous polyps that collect additional mutations (e.g. in *KRAS* and *TP53*) to develop into microsatellite-stable CRC characterized by chromosomal instability (CIN) (Fearon and Vogelstein, 1990). Recently, an alternative pathway emerged, in which colorectal cancer arises from serrated precursor polyps that are initiated by *BRAF* or *KRAS* mutations and display combined features of fetal gene expression, differentiated cells and gastric metaplasia (Patai *et al.*, 2013; Chen *et al.*, 2021). Whether and how *Lkb1* loss drives entry into one of these pathways for CRC malignant progression is not known.

To investigate this issue, we examined expression of gene sets linked to the conventional and serrated pathways of CRC development in *Lkb1*-deficient organoids (Chen *et al.*, 2021). Strikingly, all *Lkb1*-deficient organoids display significant enrichment of genes that were previously found to mark neoplastic populations of serrated-specific cells (SSC) (Figure 7A, Figure S5A-B). These effects gradually increased with the number of lost *Lkb1* alleles, along with a simultaneous decrease in the expression of adenoma-

specific genes (ASC) (Figure 7B). Single cell analysis further revealed that the serrated gene program was selectively increased in *Lkb1*-deficient stem cell populations (Figure S5C-E). Furthermore, *Lkb1*$^{cys\ -/-}$ organoids lose expression of the intestinal transcription factor *Cdx2* and upregulate expression of common gastric markers like *Aqp5*, *Tacstd2* [*Trop2*], *Tff2*, and *Msln* (Figure 7B, Supplementary Table 1), indicating that *Lkb1* loss promotes intestinal-to-gastric cellular transdifferentiation, often referred to as gastric metaplasia (Balbinot *et al.*, 2018; Chen *et al.*, 2021).

To investigate how an *Lkb1*-deficient epithelial state cooperates with common cancer mutations in CRC, we introduced *Apc* or *Kras* mutations in *Lkb1*-mutant organoids. Truncating *Apc* mutations are linked to the classical adenoma sequence, while *Kras* mutations are observed in both pathways (Fearon and Vogelstein, 1990; Patai *et al.*, 2013). As expected, based on earlier reports, introduction of a truncating *Apc* mutation induced cystic morphologies of all organoids (Figure S6A-B) (Sato, Stange, *et al.*, 2011; Dow *et al.*, 2015). Surprisingly, however, introduction of a G12D *Kras* mutation in *Lkb1*-deficient organoids also consistently mediated transition to a cystic morphology, while single *Kras*-mutant organoids maintained their crypt-villus organization (Figure S6C-D). Functionally, *Kras* mutations conveyed synergistic effects on the ability of single *Lkb1*$^{-/-}$ cells to reconstitute organoid growth (Figure 7C). By contrast, *Apc* mutations did not add any significant synergy to the reconstitution capacity of *Lkb1*$^{-/-}$ organoids (Figure 7D).

To investigate how *Apc* or *Kras* mutations alter the phenotypic landscape of intestinal epithelial organoids that already lost one or two copies of *Lkb1*, we examined transcriptional expression profiles of double mutant organoid lines using bulk mRNA sequencing and compared them to their *Lkb1*-mutant counterparts (Supplementary Table 3). With the introduction of mutant *Apc,* a slight increase was observed in fetal and SSC gene programs in both *Lkb1*$^{+/-}$ and *Lkb1*$^{-/-}$ organoids, although the expression of stem cell and ASC genes remained high for this mutational combination (Figure 7E, Figure S6E). By contrast, introduction of mutant *Kras* in *Lkb1*$^{+/-}$ or *Lkb1*$^{bud\ -/-}$ backgrounds induced a strong shift towards expression of fetal and SSC genes, while stem and ASC genes were downregulated, to a similar extent as observed for *Lkb1*$^{cys\ -/-}$ organoids (Figure 7E, Figure S6E). In *Lkb1*$^{cys\ -/-}$ organoids, introduction of mutant *Kras* did not further enhance the already strong serrated features, while introduction of truncated *Apc* in these organoids clearly suppressed the serrated state and mediated reactivation of stem and ASC gene expression. Quantification of these findings by GSEA confirmed a significant amplification of serrated signature by the introduction of *Kras* mutations in both *Lkb1*$^{+/-}$ and *Lkb1*$^{bud\ -/-}$ organoids, and downregulation of the serrated pathway by introduction of mutant Apc (Figure 7F). We conclude that *Lkb1* mutations synergize with mutant *Kras,* but not *Apc,* to drive expression of the pre-malignant serrated gene program.

To investigate the link between *Lkb1* loss and advanced serrated colorectal tumors, we examined the TCGA colorectal cancer database. First, we observed that *LKB1*-mutant tumors are significantly enriched for mutations associated with serrated cancers, including *BRAF*, *RNF43* and *PIK3CA* mutations, while *APC* mutations were significantly enriched in *LKB1* WT tumors (Figure 7G) (Day *et al.*, 2013; Robertson *et al.*, 2019). Mutations found in both classical and serrated adenocarcinomas, such as mutant *KRAS* and *TP53*, were not significantly altered between *LKB1* WT and mutant tumors (Figure 7G). We next scored TCGA colorectal samples for expression of a gene set that was upregulated in all *Lkb1*-deficient organoids. Strikingly, expression of this *Lkb1*-deficient gene signature correlated with a mucinous histological CRC subtype that is often found in serrated adenocarcinomas (Figure 7H) (Tuppurainen *et al.*, 2005). In addition, among the consensus molecular subtypes (CMS), the serrated subtypes CMS1 and CMS4 carry significantly

higher expression of the *Lkb1*-deficient gene signature compared to the classical subtype CMS2 (Figure 7I) (Nguyen, Goel and Chung, 2020). A recent study by Joanito *et al.* redefined the CMS classification and found two epithelial intrinsic cell states in CRC samples (Joanito *et al.*, 2022). The iCMS2 state shows more characteristics of classical CRCs, while the iCMS3 state correlates with features of serrated CRCs. Using GSEA, we also found enrichment of iCMS3 transcriptional features in our *Lkb1*-deficient organoids, while the iCMS2 state was downregulated (Figure S6F).

These results indicate that *Lkb1* loss drives cancer predisposition along the serrated pathway of CRC development. *Kras* activating mutations cooperate with *Lkb1* loss by amplifying the serrated state. Furthermore, upon homozygous *Lkb1* loss, a fraction of mutant cells grows out into *Lkb1*$^{cys\ -/-}$ organoids that achieve an advanced serrated state without additional oncogenic mutations. Together, these findings suggest that loss of *LKB1* converts intestinal epithelial cells in a pre-malignant state that primes for progression along the serrated pathway.

## Discussion

Over recent years, a variety of *Lkb1*-deficient mouse models have faithfully mimicked intestinal hamartomatous polyp formation as a hallmark for PJS disease. The combined findings have promoted a view in which non-epithelial functions of *LKB1* contribute to PJS disease development (Katajisto *et al.*, 2008; Ollila *et al.*, 2018; Poffenberger *et al.*, 2018; Cotton *et al.*, 2022). Despite this progress, the relationship between *LKB1* loss-induced hamartomatous polyposis and epithelial cancer predisposition has remained highly debated and, moreover, does not explain cancer development in extra-intestinal epithelia (Shepherd, Bussey and Jass, 1987; Entius *et al.*, 2001; De Leng *et al.*, 2003; Van Lier *et al.*, 2010; Korsse *et al.*, 2013). Furthermore, how heterozygous and homozygous loss of *LKB1* mediates dose-dependent alterations in PJS epithelial tissue organization at the single cell level has not been addressed, leaving the underlying cancer driver mechanisms and pathways obscure.

Here, we employed mouse small intestinal organoids, an epithelium-only culture system, to obtain an in-depth understanding of how *Lkb1* loss affects intestinal epithelial homeostatic cell identities and examine how these alterations drive the epithelium into a pre-malignant state for colorectal cancer formation. By generating both heterozygous and homozygous knockouts of *Lkb1*, we aimed to model aspects of cancer predisposition and development in PJS patients, as over 64% of PJS-derived carcinomas present inactivation of the second copy of the gene (Entius *et al.*, 2001; De Leng *et al.*, 2003). Our findings argue that heterozygous *Lkb1* loss in the intestinal epithelium is sufficient to push cells into a premalignant program for tumor development along the serrated colorectal cancer pathway, by a mechanism independent of the micro-environment. Furthermore, expression of the serrated premalignant program is amplified upon loss of the second allele. These results thus reveal that heterozygous *Lkb1*-mutant PJS epithelia already have undergone alterations in phenotypic cellular identities in comparison to healthy individuals and supports the view that loss of the second allele is a driver of cancer formation.

Our organoid-based model further confirms the previously described link between *Lkb1* loss and aberrant secretory cell specification *in vivo* in mice, indicating that our epithelium-only model faithfully reproduces the *in vivo* epithelium. We observed an increase in goblet cell numbers and mucus formation and identified secretory cells that display ‘intermediate’ features, based both on morphology and transcriptome analysis. In line with these findings, we show that expression of our newly identified *Lkb1*-deficient gene

signature correlates with a mucinous histological subtype of sporadic colorectal cancer cases. Together, these findings indicate a common link between early premalignant alterations in secretory cell type specification and colorectal cancer subtype progression. Similar *Lkb1* loss-induced alterations in secretory cell identities may play a role in other epithelial tissues, as mucinous carcinomas in different organs were frequently reported in PJS patients (Sato *et al.*, 2001; Osoegawa *et al.*, 2011; Collet *et al.*, 2020). If and how aberrant secretory cell specification may facilitate cancer development however remains an issue for further investigation.

Besides the observed alteration in secretory cell identities, transcriptomic analysis revealed that *Lkb1* loss induces an allele dosage-dependent expression of a regenerative epithelial program. Notably, activation of this tissue repair program occurred in regular culture conditions where no intestinal epithelial damage was induced. We conclude that the *Lkb1*-deficient epithelium resides in a persistent regenerative state, a condition that is worsened by loss-of-heterozygosity. A chronic state of regeneration may contribute to an increase in tumor development as exemplified by the increased incidence of colorectal cancer formation in patients suffering from inflammatory bowel disease (Lutgens *et al.*, 2013). As part of the induced regenerative/YAP signaling-dependent program, the *Lkb1*-deficient epithelium showed an increase in transcriptional expression of the *Egf* receptor family and its ligands, which allowed them to grow in the absence of Egf supplementation, a condition that is not tolerated by healthy small intestinal organoids. These findings thus reveal that the regenerative growth state induced by *Lkb1* loss endows the intestinal epithelium with niche-independent properties, which is regarded as a hallmark of cancer (Hanahan and Weinberg, 2011). Furthermore, these results provide an explanation of the previously reported expanded proliferative zone observed in the intestines of PJS patients (De Leng *et al.*, 2007)

Importantly, we uncovered that *Lkb1* loss predisposes the intestinal epithelium to express a gene program related to the serrated pathway for colorectal cancer formation. In support of these observations, *Lkb1* loss induced common features of early serrated lesions such as gastric metaplasia, induction of a regenerative gene program and depletion of classical adult stem cells (Chen *et al.*, 2021). Furthermore, inspection of a large set of sporadic colorectal cancer cases revealed that *LKB1* mutations frequently co-occur with driver mutations linked to the serrated colorectal cancer pathway. Additionally, we observed elevated expression of our *Lkb1*-deficient gene signature in the serrated colorectal cancer subtypes CMS1 and CMS4. Together, these findings thus suggest that the pathways employed for colorectal cancer development in PJS patients are strikingly different from the well-studied cancer driver events in familial adenomatous polyposis (FAP) patients that develop conventional *APC*-mutant adenocarcinomas (Li *et al.*, 2020).

Based on the work of Chen and colleagues (Chen *et al.*, 2021) a model was proposed in which different environmental triggers, such as microbial dysbiosis and a subsequent MAPK pathway activation drive the formation of sessile serrated lesions (IJspeert and Dekker, 2022; Shields *et al.*, 2022). In line with this model, we observe that introduction of oncogenic mutant *Kras* in *Lkb1*-deficient organoids amplifies serrated features and synergistically cooperates with *Lkb1* loss for organoid-forming capacity. Furthermore, our results reveal that *Lkb1* loss-of-heterozygosity induces two distinct organoid phenotypes with either a crypt-villus organization or a cystic morphology accompanied with strongly induced serrated features. Since both *Lkb1*$^{-/-}$ organoid types carried similar *Lkb1* mutations (Figure S1C), we speculate that an external stressor, such as the CRISPR procedure or clonal outgrowth, may promote this switch to a highly serrated

cystic phenotype. Although the responsible molecular triggers remain to be identified, our findings indicate that *Lkb1*$^{-/-}$ cells are sensitized to undergo such a phenotypic switch and adopt a pre-malignant growth state. Based on our findings, we conclude that the *Lkb1*-mutant epithelium is primed for the sessile serrated cancer pathway and not the conventional adenoma-to-carcinoma sequence. In line with this reasoning, the introduction of *Apc* mutations in *Lkb1*-deficient organoids did not display synergistic effects on pre-malignant transcriptional features or organoid reconstitution capacity. Together, our findings suggest that the PJS epithelium is sensitized to events that synergistically drive cells into a premalignant serrated state, such as intestinal damage or activating mutations in MAPK pathway components.

PJS patients undergo extensive and life-long monitoring in the clinic, to resect obstructive polyps and screen for (pre)cancerous lesions. Our results argue that monitoring of PJS patients will require specific screening for the occurrence of serrated lesions that potentially may occur in non-polyp regions as well. Serrated lesions are known to be frequently overlooked as their diagnosis relies on the existence of an architecturally distorted serrated crypt that are difficult to identify with regular screening methods (Rosty *et al.*, 2012). Diagnosed serrated lesions may be confirmed by various biomarkers including an increased MUC5AC expression linked to the absence of CDX2 (Chen *et al.*, 2021), or the usage of additional markers identified in this study such as ANXA1.

Taken together, our study reveals that intestinal organoids comprise a valuable model for *LKB1* mutation-induced alterations in epithelial organization and growth in PJS patients. Our findings further establish that induction of a premalignant sessile serrated program is a hallmark of PJS disease and provides an explanation for increased cancer incidence in PJS patients. The presented models may provide a starting point to uncover which and how additional mutations and environmental stressors synergistically cooperate with *LKB1* mutations, and how interactions with stromal and immune components contribute to the initiation of malignant growth of the PJS epithelium. Ultimately, in-depth knowledge on the pathways and processes involved in driving PJS epithelia into a pre-malignant state may help to design strategies that re-establish epithelial homeostasis and reduce the incidence of cancer development in PJS patients.

## References


Ayyaz, A. *et al.* (2019) 'Single-cell transcriptomes of the regenerating intestine reveal a revival stem cell', *Nature*. Springer US, 569(7754), pp. 121–125. doi: 10.1038/s41586-019-1154-y.

Baas, A. F. *et al.* (2004) 'Complete Polarization of Single Intestinal Epithelial Cells upon Activation of LKB1 by STRAD', *Cell*. Cell Press, 116(3), pp. 457–466. doi: 10.1016/S0092-8674(04)00114-X.

Balbinot, C. *et al.* (2018) 'The Cdx2 homeobox gene suppresses intestinal tumorigenesis through non-cell-autonomous mechanisms', *Journal of Experimental Medicine*, 215(3), pp. 911–926. doi: 10.1084/jem.20170934.

Bansil, R. and Turner, B. S. (2018) 'The biology of mucus: Composition, synthesis and organization', *Advanced Drug Delivery Reviews*. Elsevier, 124, pp. 3–15. doi: 10.1016/J.ADDR.2017.09.023.

Barker, N. *et al.* (2007) 'Identification of stem cells in small intestine and colon by marker gene Lgr5', *Nature 2007 449:7165*. Nature Publishing Group, 449(7165), pp. 1003–1007. doi: 10.1038/nature06196.

Beggs, A. D. *et al.* (2010) 'Peutz-Jeghers syndrome: a systematic review and recommendations for management.', *Gut*. England, 59(7), pp. 975–986. doi: 10.1136/gut.2009.198499.

Butler, A. *et al.* (2018) 'Integrating single-cell transcriptomic data across different conditions, technologies, and species', *Nature Biotechnology*, 36(5), pp. 411–420. doi: 10.1038/nbt.4096.

Candelli, T. *et al.* (2018) 'Sharq, A versatile preprocessing and QC pipeline for Single Cell RNA-seq', *bioRxiv*, p. 250811. doi: 10.1101/250811.

Chen, B. *et al.* (2021) 'Differential pre-malignant programs and microenvironment chart distinct paths to malignancy in human colorectal polyps', *Cell*. The Authors, 184(26), pp. 6262-6280.e26. doi: 10.1016/j.cell.2021.11.031.

Collet, L. *et al.* (2020) 'Kras and Lkb1 mutations synergistically induce intraductal papillary mucinous neoplasm derived from pancreatic duct cells', *Gut*. BMJ Publishing Group, 69(4), pp. 704–714. doi: 10.1136/GUTJNL-2018-318059.

Cotton, J. L. *et al.* (2022) 'PTEN and LKB1 are differentially required in Gli1-expressing mesenchymal cells to suppress gastrointestinal polyposis', *Cell Reports*, 40(3), p. 111125. doi: 10.1016/J.CELREP.2022.111125.

Day, F. L. *et al.* (2013) 'PIK3CA and PTEN gene and exon mutation-specific clinicopathologic and molecular associations in Colorectal cancer', *Clinical Cancer Research*. American Association for Cancer Research, 19(12), pp. 3285–3296. doi: 10.1158/1078-0432.CCR-12-3614/85568/AM/PIK3CA-AND-PTEN-GENE-AND-EXON-MUTATION-SPECIFIC.

Dow, L. E. *et al.* (2015) 'Apc Restoration Promotes Cellular Differentiation and Reestablishes Crypt Homeostasis in Colorectal Cancer', *Cell*. Cell Press, 161(7), pp. 1539–1552. doi: 10.1016/j.cell.2015.05.033.

Entius, M. M. *et al.* (2001) 'Molecular genetic alterations in hamartomatous polyps and carcinomas of patients with Peutz-Jeghers syndrome', *Journal of clinical pathology*, 54(2), pp. 126–131. doi:

10.1136/jcp.54.2.126.

Fearon, E. R. and Vogelstein, B. (1990) ‘A genetic model for colorectal tumorigenesis.’, *Cell*, 61(5), pp. 759–67. doi: 10.1016/0092-8674(90)90186-i.

Fodde, R. (2002) ‘The APC gene in colorectal cancer’, *European Journal of Cancer*. Pergamon, 38(7), pp. 867–871. doi: 10.1016/S0959-8049(02)00040-0.

Fordham, R. P. *et al.* (2013) ‘Transplantation of expanded fetal intestinal progenitors contributes to colon regeneration after injury’, *Cell Stem Cell*. The Authors, 13(6), pp. 734–744. doi: 10.1016/j.stem.2013.09.015.

Fujii, M. *et al.* (2015) ‘Efficient genetic engineering of human intestinal organoids using electroporation’, *Nature Protocols 2015 10:10*. Nature Publishing Group, 10(10), pp. 1474–1485. doi: 10.1038/nprot.2015.088.

Fujii, M. *et al.* (2016) ‘A Colorectal Tumor Organoid Library Demonstrates Progressive Loss of Niche Factor Requirements during Tumorigenesis’, *Cell Stem Cell*. Cell Press, 18(6), pp. 827–838. doi: 10.1016/J.STEM.2016.04.003.

Gao, Y. *et al.* (2020) ‘LKB1 Represses ATOH1 via PDK4 and Energy Metabolism and Regulates Intestinal Stem Cell Fate’, *Gastroenterology*. W.B. Saunders, 158(5), p. 1401. doi: 10.1053/j.gastro.2019.12.033.

Giardiello, F. M. *et al.* (2000) ‘Very high risk of cancer in familial Peutz-Jeghers syndrome.’, *Gastroenterology*. United States, 119(6), pp. 1447–1453. doi: 10.1053/gast.2000.20228.

Giardiello, F. M. and Trimbath, J. D. (2006) ‘Peutz-Jeghers syndrome and management recommendations.’, *Clinical gastroenterology and hepatology: the official clinical practice journal of the American Gastroenterological Association*. United States, 4(4), pp. 408–415. doi: 10.1016/j.cgh.2005.11.005.

Gregorieff, A. *et al.* (2015) ‘Yap-dependent reprogramming of Lgr5+ stem cells drives intestinal regeneration and cancer’, *Nature*, 526(7575), pp. 715–718. doi: 10.1038/nature15382.

Haber, A. L. *et al.* (2017) ‘A single-cell survey of the small intestinal epithelium’, *Nature*. Nature Publishing Group, 551(7680), pp. 333–339. doi: 10.1038/nature24489.

Hafemeister, C. and Satija, R. (2019) ‘Normalization and variance stabilization of single-cell RNA-seq data using regularized negative binomial regression’, *Genome Biology*. Genome Biology, 20(1), pp. 1–15. doi: 10.1186/s13059-019-1874-1.

Hanahan, D. and Weinberg, R. A. (2011) ‘Hallmarks of Cancer: The Next Generation’, *Cell*. Cell Press, 144(5), pp. 646–674. doi: 10.1016/J.CELL.2011.02.013.

Hanemaaijer, E. S. *et al.* (2021) ‘Single-cell atlas of developing murine adrenal gland reveals relation of Schwann cell precursor signature to neuroblastoma phenotype’, *Proceedings of the National Academy of Sciences of the United States of America*, 118(5). doi: 10.1073/pnas.2022350118.

He, G.-W. *et al.* (2022) ‘Optimized human intestinal organoid model reveals interleukin-22-dependency of paneth cell formation’, *Cell Stem Cell*, 29. doi: 10.1016/j.stem.2022.08.002.

Hearle, N. *et al.* (2006) ‘Frequency and spectrum of cancers in the Peutz-Jeghers syndrome.’, *Clinical cancer research□: an official journal of the American Association for Cancer Research*. United States, 12(10), pp. 3209–3215. doi: 10.1158/1078-0432.CCR-06-0083.

Hemminki, A. *et al.* (1998) ‘A serine/threonine kinase gene defective in Peutz–Jeghers syndrome’, *Nature 1998 391:6663*. Nature Publishing Group, 391(6663), pp. 184–187. doi: 10.1038/34432.

IJspeert, J. E. G. and Dekker, E. (2022) ‘Gastric metaplasia could initiate the serrated neoplasia pathway in CRC’, *Nature Reviews Gastroenterology and Hepatology*, 19(4), pp. 217–218. doi: 10.1038/s41575-022-00592-z.

Jenne, D. E. *et al.* (1998) ‘Peutz-Jeghers syndrome is caused by mutations in a novel serine threoninekinase’, *Nature Genetics 1998 18:1*. Nature Publishing Group, 18(1), pp. 38–43. doi: 10.1038/ng0198-38.

Joanito, I. *et al.* (2022) ‘Single-cell and bulk transcriptome sequencing identifies two epithelial tumor cell states and refines the consensus molecular classification of colorectal cancer’, *Nature Genetics*, 54(7), pp. 963–975. doi: 10.1038/s41588-022-01100-4.

Katajisto, P. *et al.* (2008) ‘LKB1 signaling in mesenchymal cells required for suppression of gastrointestinal polyposis’, *Nature genetics*. Nat Genet, 40(4), pp. 455–459. doi: 10.1038/NG.98.

Kim, Y. *et al.* (2022) ‘LKB1 in Intestinal Epithelial Cells Regulates Bile Acid Metabolism by Modulating FGF15/19 Production’, *Cmgh*, 13(4), pp. 1121–1139. doi: 10.1016/j.jcmgh.2021.12.017.

Kline, E. R. *et al.* (2013) ‘LKB1 Represses Focal Adhesion Kinase (FAK) Signaling via a FAK-LKB1 Complex to Regulate FAK Site Maturation and Directional Persistence’, *The Journal of Biological Chemistry*. American Society for Biochemistry and Molecular Biology, 288(24), p. 17663. doi: 10.1074/JBC.M112.444620.

Korsse, S. E. *et al.* (2013) ‘Identification of molecular alterations in gastrointestinal carcinomas and dysplastic hamartomas in Peutz-Jeghers syndrome’, *Carcinogenesis*. Oxford Academic, 34(7), pp. 1611–1619. doi: 10.1093/CARCIN/BGT068.

De Leng, W. W. J. *et al.* (2003) ‘Cyclooxygenase 2 expression and molecular alterations in Peutz-Jeghers hamartomas and carcinomas.’, *Clinical cancer research□: an official journal of the American Association for Cancer Research*. United States, 9(8), pp. 3065–72. Available at: http://www.ncbi.nlm.nih.gov/pubmed/12912958.

De Leng, W. W. J. *et al.* (2007) ‘Peutz–Jeghers syndrome polyps are polyclonal with expanded progenitor cell compartment’, *Gut*. BMJ Publishing Group, 56(10), pp. 1475–1476. doi: 10.1136/GUT.2007.128132.

Li, J. *et al.* (2020) ‘Genomic and transcriptomic profiling of carcinogenesis in patients with familial adenomatous polyposis’, *Gut*, 69, pp. 1283–1293. doi: 10.1136/gutjnl-2019-319438.

Van Lier, M. G. F. *et al.* (2010) ‘High cancer risk in peutz-jeghers syndrome: A systematic review and surveillance recommendations’, *American Journal of Gastroenterology*. Nature Publishing Group, 105(6), pp. 1258–1264. doi: 10.1038/ajg.2009.725.

Lutgens, M. W. M. D. *et al.* (2013) 'Declining Risk of Colorectal Cancer in Inflammatory Bowel DiseaseAn Updated Meta-analysis of Population-based Cohort Studies', *Inflammatory Bowel Diseases*. Oxford Academic, 19(4), pp. 789–799. doi: 10.1097/MIB.0B013E31828029C0.

Merenda, A., Fenderico, N. and Maurice, M. M. (2020) 'Wnt Signaling in 3D: Recent Advances in the Applications of Intestinal Organoids Trends in Cell Biology', *Trends in Cell Biology*, 30(1). doi: 10.1016/j.tcb.2019.10.003.

Mohseni, M. *et al.* (2014) 'A genetic screen identifies an LKB1-MARK signalling axis controlling the Hippo-YAP pathway', *Nature Cell Biology*. Nature Publishing Group, 16(1), pp. 108–117. doi: 10.1038/ncb2884.

Muraro, M. J. *et al.* (2016) 'A Single-Cell Transcriptome Atlas of the Human Pancreas', *Cell Systems*. Elsevier, 3(4), p. 385. doi: 10.1016/J.CELS.2016.09.002.

Mustata, R. C. *et al.* (2013) 'Identification of Lgr5-Independent Spheroid-Generating Progenitors of the Mouse Fetal Intestinal Epithelium', *Cell Reports*, 5(2), pp. 421–432. doi: 10.1016/j.celrep.2013.09.005.

Nguyen, L. H., Goel, A. and Chung, D. C. (2020) 'Pathways of Colorectal Carcinogenesis', *Gastroenterology*. Elsevier, Inc, 158(2), pp. 291–302. doi: 10.1053/j.gastro.2019.08.059.

Nusse, Y. M. *et al.* (2018) 'Parasitic helminths induce fetal-like reversion in the intestinal stem cell niche', *Nature*. Springer US, 559(7712), pp. 109–113. doi: 10.1038/s41586-018-0257-1.

Ollila, S. *et al.* (2018) 'Stromal Lkb1 deficiency leads to gastrointestinal tumorigenesis involving the IL-11-JAK/STAT3 pathway', *The Journal of clinical investigation*. J Clin Invest, 128(1), pp. 402–414. doi: 10.1172/JCI93597.

Osoegawa, A. *et al.* (2011) 'LKB1 Mutations Frequently Detected in Mucinous Bronchioloalveolar Carcinoma', *Japanese Journal of Clinical Oncology*. Oxford Academic, 41(9), pp. 1132–1137. doi: 10.1093/JJCO/HYR102.

Patai, Á. V. *et al.* (2013) 'Serrated pathway: Alternative route to colorectal cancer', *World Journal of Gastroenterology*, 19(5), pp. 607–615. doi: 10.3748/wjg.v19.i5.607.

Pierce, S. E. *et al.* (2021) 'LKB1 inactivation modulates chromatin accessibility to drive metastatic progression', *Nature Cell Biology*, 23(8), pp. 915–924. doi: 10.1038/s41556-021-00728-4.

Poffenberger, M. C. *et al.* (2018) 'LKB1 deficiency in T cells promotes the development of gastrointestinal polyposis', *Science*. American Association for the Advancement of Science, 361(6400), pp. 406–411. doi: 10.1126/SCIENCE.AAN3975.

Qu, M. *et al.* (2021) 'Establishment of intestinal organoid cultures modeling injury-associated epithelial regeneration', *Cell Research*. Springer US, 31(3), pp. 259–271. doi: 10.1038/s41422-020-00453-x.

Ran, F. A. *et al.* (2013) 'Genome engineering using the CRISPR-Cas9 system', *Nature Protocols*, 8(11), pp. 2281–2308. doi: 10.1038/nprot.2013.143.

Ren, F. *et al.* (2010) 'Hippo signaling regulates Drosophila intestine stem cell proliferation through multiple pathways', *Proceedings of the National Academy of Sciences of the United States of America*. National

Academy of Sciences, 107(49), pp. 21064–21069. doi: 10.1073/PNAS.1012759107/SUPPL_FILE/PNAS.201012759SI.PDF.

Robertson, D. J. *et al.* (2019) 'Terminology, Molecular Features, Epidemiology, and Management of Serrated Colorectal Neoplasia', *Gastroenterology*. Elsevier, 157(4), pp. 949-966.e4. doi: 10.1053/J.GASTRO.2019.06.041.

Rosty, C. *et al.* (2012) 'Serrated polyps of the large intestine: current understanding of diagnosis, pathogenesis, and clinical management', *Journal of Gastroenterology 2012 48:3*. Springer, 48(3), pp. 287–302. doi: 10.1007/S00535-012-0720-Y.

Sanchez-Cespedes, M. (2007) 'A role for LKB1 gene in human cancer beyond the Peutz-Jeghers syndrome.', *Oncogene*. England, 26(57), pp. 7825–7832. doi: 10.1038/sj.onc.1210594.

Sato, N. *et al.* (2001) 'STK11/LKB1 Peutz-Jeghers Gene Inactivation in Intraductal Papillary-Mucinous Neoplasms of the Pancreas', *The American Journal of Pathology*. Elsevier, 159(6), pp. 2017–2022. doi: 10.1016/S0002-9440(10)63053-2.

Sato, T. *et al.* (2009) 'Single Lgr5 stem cells build crypt-villus structures in vitro without a mesenchymal niche', *Nature*. Macmillan Publishers Limited. All rights reserved, 459(7244), pp. 262–265. doi: 10.1038/nature07935.

Sato, T., Stange, D. E., *et al.* (2011) 'Long-term Expansion of Epithelial Organoids From Human Colon, Adenoma, Adenocarcinoma, and Barrett's Epithelium', *Gastroenterology*. W.B. Saunders, 141(5), pp. 1762–1772. doi: 10.1053/J.GASTRO.2011.07.050.

Sato, T., Es, J. H. Van, *et al.* (2011) 'Paneth cells constitute the niche for Lgr5 stem cells in intestinal crypts', *Nature*, 469(7330), pp. 415–418. doi: 10.1038/nature09637.Paneth.

Satoh, Y. *et al.* (1990) 'Ultrastructure of Paneth cells in the intestine of various mammals', *Journal of Electron Microscopy Technique*. John Wiley & Sons, Ltd, 16(1), pp. 69–80. doi: 10.1002/JEMT.1060160109.

Shackelford, D. B. and Shaw, R. J. (2009) 'The LKB1-AMPK pathway: Metabolism and growth control in tumour suppression', *Nature Reviews Cancer*. Nature Publishing Group, 9(8), pp. 563–575. doi: 10.1038/nrc2676.

Shepherd, N. A., Bussey, H. J. and Jass, J. R. (1987) 'Epithelial misplacement in Peutz-Jeghers polyps. A diagnostic pitfall.', *The American journal of surgical pathology*, 11(10), pp. 743–9. doi: 10.1097/00000478-198710000-00001.

Shields, C. E. D. *et al.* (2022) 'Sensitive To Immune Checkpoint Therapy', 11(7), pp. 1792–1807. doi: 10.1158/2159-8290.CD-20-0770.Bacterial-driven.

Shorning, B. Y. *et al.* (2009) 'Lkb1 deficiency alters goblet and paneth cell differentiation in the small intestine.', *PloS one*. Edited by R. E. Morty, 4(1), p. e4264. doi: 10.1371/journal.pone.0004264.

Tomasetti, C. and Vogelstein, B. (2015) 'Variation in cancer risk among tissues can be explained by the number of stem cell divisions', *Science*. American Association for the Advancement of Science, 347(6217),

pp. 78–81. doi: 10.1126/SCIENCE.1260825.

Troughton, W. D. and Trier, J. S. (1969) ‘Paneth and goblet cell renewal in mouse duodenal crypts.’, *The Journal of cell biology*, 41(1), pp. 251–268. doi: 10.1083/jcb.41.1.251.

Tuppurainen, K. *et al.* (2005) ‘Morphology and microsatellite instability in sporadic serrated and non-serrated colorectal cancer’, *Journal of Pathology J Pathol*, 207, pp. 285–294. doi: 10.1002/path.1850.

Wang, Y. *et al.* (2019) ‘Long-Term Culture Captures Injury-Repair Cycles of Colonic Stem Cells’, *Cell*. Elsevier Inc., 179(5), pp. 1144-1159.e15. doi: 10.1016/j.cell.2019.10.015.

Yang, N. *et al.* (2012) ‘TAZ induces growth factor-independent proliferation through activation of EGFR ligand amphiregulin’, *Cell Cycle*. Taylor and Francis Inc., 11(15), pp. 2922–2930. doi: 10.4161/CC.21386.

Yui, S., Azzolin, L., Maimets, M., Pedersen, M. T., Fordham, R. P., Hansen, S. L., Larsen, H. L., Guiu, J., Alves, M. R. P., *et al.* (2018) ‘YAP/TAZ-Dependent Reprogramming of Colonic Epithelium Links ECM Remodeling to Tissue Regeneration’, *Cell Stem Cell*. Cell Press, 22(1), pp. 35-49.e7. doi: 10.1016/j.stem.2017.11.001.

Zhang, J. *et al.* (2009) ‘YAP-dependent induction of amphiregulin identifies a non-cell-autonomous component of the Hippo pathway’, *Nature Cell Biology*. doi: 10.1038/ncb1993.

## Figure legends

**Figure 1. *Lkb1*-deficient organoids show heterogeneous morphology and viability.**
**A)** Representative brightfield images of mouse small intestine *Lkb1*-deficient organoid clones. Lower panel images show zoom-in images of boxed area in upper panel images. Scale = 100 µM **B)** Western blot analysis of Lkb1 protein levels in WT and *Lkb1*-deficient organoids. **C)** Organoid reconstitution assay from single cells performed at day 7. One-way ANOVA (Dunnett) was applied for analysis. * = $p < 0.05$. Each dot represents a biological replicate, $N = 16$. **D)** Representative images of an EdU incorporation (magenta) experiment marking the proliferative compartments in wild-type (WT) and *Lkb1*-deficient organoids. **E)** Quantification of $EdU^+$ cells over the total number of cells ($DAPI^+$ cells) of *Lkb1*-deficient organoids. For each condition, $N = 1000$ cells were analyzed derived from one independent experiment.

**Figure 2. *Lkb1* loss alters the number, location and granule composition of secretory cells. A)** Representative images of immunostaining for Lysozyme1 (Lyz1, green) to detect $Lyz1^+$ cells in *Lkb1*-deficient clones. Cellular membranes are visualized using F-actin (white). Images are max projections of z-stack. Scale bar = 25 µm. White arrows indicate mislocalized $Lyz1^+$ cells. **B)** Representative images of immunohistochemistry staining of Mucin 2 (Muc2) to visualize $Muc2^+$ cells in *Lkb1*-deficient clones. Scale bar = 100 µm. **C-D)** Representative images of MUC2 **(C)** and LYZ1 **(D)** staining to visualize the localization of $MUC2^+$ and $LYZ1^+$ cells respectively in healthy intestinal epithelium and non-transformed PJS epithelium. Arrows indicate mislocalized $LYZ1^+$ cells. Scalebar = 100 µm. **E)** Representative images of electron microscopy comparing the ultrastructure of Paneth cells and their secretory granules in wild-type organoids and *Lkb1*-deficient organoids. Lower panel images show zoom-in images of boxed area in upper panel images. Scale bar upper panels = 5 µm, scale bar lower panels = 1 µm. **F)** Representative images of electron microscopy comparing the ultrastructure of goblet cells and their secretory granules in wild-type organoids and *Lkb1*-deficient organoids. Lower panel images show zoom-in images of boxed area in upper panel images. Scale bar upper panels = 5 µm, scale bar lower panels = 1 µm.

**Figure 3. *Lkb1* loss upregulates a regenerative gene signature in the intestinal epithelium. A)** *Lkb1*-deficient versus wild-type (WT) organoid derived bulk mRNA-seq sequencing data was analyzed by gene set enrichment analysis (GSEA) for cell types (Haber *et al.*, 2017), colitis (Yui, Azzolin, Maimets, Pedersen, Fordham, Hansen, Larsen, Guiu, M. R. P. Alves, *et al.*, 2018), injury (Qu *et al.*, 2021), parasite (Nusse *et al.*, 2018), fetal spheroid (Mustata *et al.*, 2013), Yap regeneration (Gregorieff *et al.*, 2015) and revival stem cell (Ayyaz *et al.*, 2019) gene sets. The normalized enrichment score (NES) is depicted on the X-axis and the false discovery rates (FDRs) is indicated by the size of the dots. The color of the lines reflects whether a signature is enriched in WT (red) or *Lkb1*-deficient (blue) organoids. The shape of the dot (open/closed) indicates whether a signature is significantly enriched (FDR < 0.05). **B)** Heatmap of z-score transformed expression values of $Lgr5^+$ stem cell genes (Stem) (Haber *et al.*, 2017) enriched in WT organoids (top cluster) and fetal genes (Fetal) (Mustata *et al.*, 2013) enriched in *Lkb1*-deficient organoids (bottom cluster). Key marker genes are highlighted. Each column represents a biological replicate of the indicated group, N = 3. **C)** Representative images of immunofluorescent staining to detect expression of the fetal marker Anxa1 (green) in *Lkb1*-deficient clones. Embryonic spheroids from E16.5 mice were used as positive control.

Cellular membranes are visualized by F-actin (red) and nuclei by DAPI (blue). **D)** Representative images of immunohistochemistry staining of the fetal marker ANXA1 in healthy intestinal epithelium, PJS non-transformed epithelium and PJS dysplastic tissue. High magnification of the area indicated by black arrows is shown in the upper right corner. Scale bar = 100 µm

**Figure 4. *Lkb1*-deficient organoids show a Yap-induced regenerative state.**

**A)** Representative images of immunofluorescent staining of Yap (green) in wild-type (WT) and *Lkb1*-deficient organoids. Nuclei are visualized by DAPI staining (blue). High magnification of the area indicated by white box is shown in the lower three panels. Scale bar = 20 µm. **B)** Quantification of the nuclear fraction of Yap. Dots represent individual organoids derived from two independent experiments. *N* = 5 for WT organoids, *N* = 7 for $Lkb1^{+/-}$ organoids, *N* = 7 for $Lkb1^{bud\ -/-}$ organoids and *N* = 7 for $Lkb1^{cys\ -/-}$. One-way ANOVA was applied for analysis and statistical significance was defined as ** = p < 0.05, ** = p < 0.01 and **** = p < 0.0001.*

**Figure 5. *Lkb1*-deficient organoids upregulate EGF family receptors and its ligands for niche independency.**

**A-B)** Cumulative normalized counts of *Egfr* binding ligands **(A)** and *Egf* family receptors **(B)** in wild-type (WT) and *Lkb1*-deficient organoids. One-way ANOVA was applied for analysis and statistical significance was defined as *ns = not significant, * = p < 0.05, ** = p < 0.01 and **** = p < 0.0001.* Each dot represents one biological replicate, N = 3. **C)** Representative bright field images of WT and *Lkb1*-deficient organoids grown in the presence (ENR) and absence (NR) of Egf. Organoids were incubated for 7 days in indicated medium and split on day 4. Scale bar = 500 µm. **D)** Representative bright field images of WT and *Lkb1*-deficient organoids cultured in NR and treated with DMSO or 100 nM Gefitinib. Organoids were incubated for 9 days in indicated medium and split on day 6. Scale bar = 500 µm.

**Figure 6. *Lkb1*-deficiency redefines intestinal stem cell identity.**

**A-B)** UMAP visualization of scRNA-seq data from wild-type (WT (Adult)), fetal (WT(Fetal)) and *Lkb1*-deficient organoids. Colors indicate the different organoids lines **(A)** and the different cell types **(B)**. **C)** Fraction of cell types for each organoid line. Each color indicates a different cell type, related to figure B. **D)** Scatter plot showing module scores for a Paneth gene signature (Haber *et al.*, 2017) on the y-axis and for a goblet cell signature (Haber *et al.*, 2017) on the x-axis across all cells. Color/shape indicates the origin of the single cell. **E)** Violin plot showing a module score for Egf family ligands within the goblet and enteroendocrine (EEC) cluster. Colors reflect different organoid lines. **F)** Expression of the fetal marker *Anxa1* is overlaid onto the UMAP plot for the different organoid lines. **G)** GSEA was performed on genes differentially expressed between WT and *Lkb1*-deficient stem cells for cell types (Haber *et al.*, 2017), colitis (Yui, Azzolin, Maimets, Pedersen, Fordham, Hansen, Larsen, Guiu, M. R. P. Alves, *et al.*, 2018), embryonic spheroid (Mustata *et al.*, 2013), Yap regeneration (Gregorieff *et al.*, 2015) and revival stem cell (Ayyaz *et al.*, 2019) gene sets. The normalized enrichment score (NES) is depicted on the X-axis and the false discovery rates (FDRs) are indicated by the size of the dots. The color of the lines reflects whether a signature is enriched in WT (red) or *Lkb1*-deficient (blue) organoids. The shape of the dot (open/closed) indicates whether a signature is significantly enriched (FDR < 0.05). **H)** Violin plot showing module scores for a goblet cell gene signature (Haber *et al.*, 2017) across WT stem cells, $Lkb1^{+/-}$ stem cells, $Lkb1^{bud\ -/-}$ stem cells and all $Lkb1^{cys\ -/-}$ cells. **I)**

Violin plot showing expression of the regenerative marker *Anxa1* across WT stem cells, *Lkb1*$^{+/-}$ stem cells, *Lkb1*$^{bud\ -/-}$ stem cells and all *Lkb1*$^{cys\ -/-}$ cells.

**Figure 7. *Lkb1* loss drives a pre-malignant program along the serrated pathway which can be amplified by additional *Kras* mutations. A)** GSEA was performed for a serrated-specific gene set (Chen *et al.*, 2021). The normalized enrichment score (NES) is depicted on the X-axis and the false discovery rate (FDR) is indicated by the size of the dots. The shape of the dot (open/closed) indicates whether a signature is significantly enriched (FDR < 0.05). **B)** Heatmap of z-score transformed expression values of adenoma-specific genes (ASC) (Chen *et al.*, 2021) enriched in WT organoids (top cluster) and serrated-specific genes (SSC) (Chen *et al.*, 2021) enriched in *Lkb1*-deficient organoids (bottom cluster). Each column represents a biological replicate of the indicated group, N = 3. **C)** Organoid reconstitution assay from single cells performed at day 7 from trypsinization is shown for *Apc*-deficient and *Apc/Lkb1*-deficient organoids. Each dot represents a biological replicate, *N* = 8 **D)** Cell reconstitution assay from single cells performed at day 7 from trypsinization is shown for *Kras*-mutant and *Kras*-mutant/*Lkb1*-deficient organoids. Each dot represents a biological replicate, *N* = 8 **E)** Heatmap of z-score transformed expression values of ASC genes enriched in control organoids (top cluster) and SSC genes enriched in *Lkb1*-deficient organoids (bottom cluster) for *Lkb1* single mutant (green) and *Apc/Lkb1* double mutant (blue) or *Kras*/*Lkb1* double mutant organoids (yellow). Each column represents a biological replicate of the indicated group, N = 3. **F)** GSEA of a serrated-specific gene set (Chen *et al.*, 2021) was performed on *Lkb1*-deficient and *Apc/Lkb1*-deficient or *Kras*-mutant/*Lkb1*-deficient organoids. The normalized enrichment score (NES) is depicted on the X-axis and the FDR is indicated by the size of the dots. The color of the lines reflects whether a signature is enriched in *Lkb1*-deficient (red) or *Lkb1*-deficient/*Kras*-mutant (blue) organoids. **G)** Percentage of samples mutated for *BRAF, RNF43, PIK3CA, APC, KRAS* or *TP53* in *LKB1* WT (*N* = 88) and *LKB1*-mutant (*N* = 7472) colorectal tumors according to cBioPortal. The Benjamini-Hochberg procedure was applied for analysis and statistical significance was determined as * = *FDR < 0.05, ** = FDR < 0.01 and **** = FDR < 0.0001.* **H, I)** Box plots showing log2 Z-scores for the *Lkb1*-deficient signature (genes significantly (*padj < 0.05*) upregulated in all deficient clones compared to wild type organoids) over the colon adenocarcinoma TCGA bulk RNA sequencing dataset grouped by histological classification as mucinous (*N* = 68) or non-mucinous (*N* = 437) **(H)** or consensus molecular subtype (CMS1; *N* = 63, CMS2; *N* = 125, CMS3; *N* = 45, CMS 4; *N* = 73) **(I)** Welch's unequal variances t-test was applied for analysis and statistical significance was determined as * = *p < 0.05, ** = p < 0.01 and **** = p < 0.0001.*

**Figure S1. *Lkb1* loss induced by different gRNAs results in similar heterogeneous phenotypes. A)** Sequences of *Lkb1*-deficient organoids obtained with gRNA1 showing indels/deletions detected in exon 1 of the *Lkb1* gene. PAM sequences are underlined. **B)** Immunofluorescent images showing cleaved caspase 3 staining (green) marking apoptotic cells in *Lkb1*-deficient and wild type organoids. Cellular membranes are visualized by F-actin (white). Scale bar = 33 µm. **C)** Sequences of *Lkb1*-deficient organoids obtained with gRNA2 showing indels/deletions detected in exon 1 of the *Lkb1* gene. PAM sequences are underlined. **D)** Representative brightfield images of *Lkb1*-deficient clones showing heterogeneous morphologies. **E)** Western blot analysis of Lkb1 expression in each clone. **F)** Organoid reconstitution assay from single cells

for wild type and different morphologies of Lkb1$^{-/-}$ performed at day 7 from trypsinization. Friedman test was applied for analysis. * = $p < 0.05$, * = $p < 0.01$. Each dot represents a biological replicate, $N = 5$.

**Figure S2. Goblet cell number and positioning are unaltered in PJS epithelia and *Lkb1*-deficient organoids display proper brush border formation. A-B)** The average number **(A)** and position **(B)** of goblet cells healthy and PJS epithelia. Each dot represents a single crypt. For healthy donors 40 crypts from 4 individuals were counted. For PJS untransformed epithelia 30 crypts from 3 individuals were counted. Unpaired t-test was applied for analysis. *ns* = *not significant*. **C)** Representative electron microscopy images of wild type (WT) and *Lkb1*-deficient organoids. Arrows indicate brush border formation in indicated organoid lines. A zoom-in of the area indicated by the red arrows is shown in the bottom panel. Scale bar = 2 µm.

**Figure S3. Yap target gene expression progressively increases with loss of both *Lkb1* alleles.**
**A)** GSEA was performed for *Lkb1*$^{cys\ -/-}$ organoids versus WENR treated wild-type (WT (WENR)) organoids or *Apc*$^{-/-}$ organoids. The following gene sets were tested: cell types (Haber *et al.*, 2017), colitis (Yui, Azzolin, Maimets, Pedersen, Fordham, Hansen, Larsen, Guiu, M. R. P. Alves, *et al.*, 2018), injury (Qu *et al.*, 2021), parasite (Nusse *et al.*, 2018), fetal spheroid (Mustata *et al.*, 2013), Yap regeneration (Gregorieff *et al.*, 2015) and revival stem cell (Ayyaz *et al.*, 2019). The normalized enrichment score (NES) is depicted on the X-axis and the false discovery rates (FDRs) is indicated by the size of the dots. The color of the lines reflects whether a signature is enriched in WT (WENR) (blue), *Lkb1*$^{cys\ -/-}$ (green), or *Apc*$^{-/-}$ (red) organoids. The shape of the dot (open/closed) indicates whether a signature is significantly enriched (FDR < 0.05). **B)** Heatmap of z-score transformed expression values of Yap responsive genes (Gregorieff *et al.*, 2015) enriched in *Lkb1*-deficient organoids. Key marker genes are highlighted. Each column represents a biological replicate of the indicate group, N = 3.

**Figure S4. Identification of intestinal cell types of WT and *Lkb1*-deficient organoids.**
**A)** UMAP visualization of scRNA-seq data from wild-type (WT), fetal and *Lkb1*-deficient organoids. Colors indicate different clusters as defined by Seurat analysis **B)** Expression of known markers for different cell populations in WT and *Lkb1*-deficient organoids. Size of the dot represents percentage of cells expressing marker gene and the color the average expression within that population. **C-I)** Module scores for enterocyte **(C)**, enteroendocrine **(D)**, goblet **(E)**, stem **(F)**, transit amplifying (G1) **(G)**, Paneth **(H)** and tuft **(I)** cell gene signatures (Haber *et al.*, 2017) overlaid on the UMAP plot of *Lkb1*-deficient, fetal and WT organoids. **J-K)** Reclustering of stem cell populations from WT, *Lkb1*$^{+/-}$, *Lkb1*$^{-/-\ bud}$ and *Lkb1*$^{-/-\ cys}$ organoids showing clusters as identified by Seurat analysis **(J)** and by organoid line **(K)**.

**Figure S5. Induction of serrated genes in *Lkb1*-deficient organoids is reflected at the single cell level.**
**A)** Module score for a serrated-specific (SSC) gene set (Chen *et al.*, 2021) on the UMAP plot of *Lkb1*-deficient, fetal and WT organoids. **B)** Violin plot showing a module score for a serrated-specific gene set across WT, fetal, *Lkb1*$^{+/-}$, *Lkb1*$^{bud\ -/-}$ and *Lkb1*$^{cys\ -/-}$ organoids. **C)** GSEA was performed for a serrated-specific gene set (Chen *et al.*, 2021). The normalized enrichment score (NES) is depicted on the Y-axis and the false discovery rate (FDR) is indicated by the size of the dots. Line colors reflects enrichment of the signature in WT (blue) or *Lkb1*-deficient (red) stem cells. Dot shape (open/closed) indicates significant enrichment (FDR

< 0.05). **D)** Module score for a serrated-specific gene set (Chen *et al.*, 2021) on the UMAP plot of WT stem cells, *Lkb1*$^{+/-}$ stem cells, *Lkb1*$^{bud\ -/-}$ stem cells and all *Lkb1*$^{cys\ -/-}$ cells. **E)** Violin plot showing module scores of a serrated-specific gene set (Chen *et al.*, 2021) for WT stem cells, *Lkb1*$^{+/-}$ stem cells, *Lkb1*$^{bud\ -/-}$ stem cells and all *Lkb1*$^{cys\ -/-}$ cells.

**Figure S6. *Lkb1* loss drives expression of a pre-malignant program along the serrated pathway which can be amplified by additional *Kras* mutations. A)** Representative brightfield images of *Apc* and *Apc/Lkb1*-deficient organoids. **B)** Representative brightfield images of *Kras*-mutant and *Kras*-mutant/*Lkb1*-deficient organoids. **C)** Sequences of *Apc*$^{-/-}$ and *Lkb1/Apc* mutant organoids showing indels/deletions detected in exon 15 of the *Apc* gene. PAM sequences are underlined. **D)** Sequences of *Kras*$^{G12D}$ and *Lkb1/Kras* mutant organoids showing G12D mutations/deletions detected in exon 2 of the *Kras* gene. PAM sequences are underlined. **E)** Heatmap of z-score transformed expression values of *Lgr5*$^{+}$ stem cell genes (Stem) (Haber *et al.*, 2017) enriched in control organoids (top cluster) and fetal genes (Fetal) (Mustata *et al.*, 2013) enriched in *Lkb1*-deficient organoids (bottom cluster) for *Lkb1* single mutant (green) and *Apc/Lkb1* double mutant (blue) or *Kras*/*Lkb1* double mutant organoids (yellow). Each column represents a biological replicate of the indicate group, N = 3. **F)** GSEA of iCMS2 and iCMS3 gene signatures (Joanito *et al.*, 2022) was performed on *Lkb1*-deficient organoids compared to control organoids. The normalized enrichment score (NES) is depicted on the X-axis and the FDR is indicated by the size of the dots. Line color reflects signature enrichment in *Lkb1*-deficient (red) or *Lkb1*-deficient/*Kras*-mutant (blue) organoids. Dot shape (open/closed) indicates significant enrichment (FDR < 0.05).

## Materials and Methods

### Organoid culture

Small intestinal mouse organoids were established from crypts isolated from the small intestine of wild-type mice, as previously described (Sato *et al.*, 2009). Basal culture medium for mouse organoids contained advanced DMEM/F12 (Gibco) supplemented with 1% Penicillin-Streptomycin (Sigma-Aldrich), 10 mM HEPES (Gibco), 1% Ultraglutamine 1 (Lonza), 1% B27 (Sigma-Aldrich), 0.5% N2 (Sigma-Aldrich) and 1 mM N-acetylcysteine (Sigma- Aldrich). Basal culture medium was further supplemented with murine recombinant EGF (Peprotech), 2.5% R-spondin1 conditioned medium (homemade) and 10% Noggin conditioned medium (homemade) to obtain the complete ENR (EGF-Noggin-Rspondin) medium. Organoids were grown in Matrigel (Corning) or BME (Cultrex) and passaged every 6-8 days as previously described (Sato *et al.*, 2009); their medium was refreshed every 2-3 days. For growth factor withdrawal experiments, EGF was removed from organoid culture medium and organoids were monitored for a total of 16 days. Bright field images were acquired with the Invitrogen™ EVOS™ FL Color Imaging System (Thermo Fisher Scientific). To obtain wild type cystic organoids, wild type organoids were supplemented with 50% Wnt3a-conditioned medium (homemade) and 1mM Nicotinamide (Sigma-Aldrich)

### Vectors and sgRNAs

The pSpCas9(BB)-2A-Puro plasmid was obtained from Addgene (48139). Single guide RNAs (sgRNAs) and are listed in **Table S4**. Cloning of sgRNAs into the The pSpCas9(BB)-2A-Puro plasmid was performed according to previously published protocols (Ran *et al.*, 2013) and vector sequences conformed by Sanger sequencing.

### Organoid electroporation

For electroporation, mouse organoids were expanded in ENR medium without antibiotics and supplemented with 50% Wnt3a-conditioned medium (homemade) and 1mM Nicotinamide (Sigma-Aldrich). Electroporation of organoids was performed as previously described using a NEPA21 (NEPAGENE) electroporator (Fujii *et al.*, 2015). To obtain *Lkb1*-deficient organoids, a total of 20 µg of DNA (10 µg gRNA, 7.2 µg of pPB-CAG-rtTA_Hygromycin and 2.8 µg PiggyBac transposase) was used. To obtain *Apc* and *Kras* mutant organoids a total of 10 µg DNA (gRNA and gRNA with oligonucleotide respectively) was used. 100 µg/mL Hygromycin B was used to select *Lkb1*-deficient organoids and Noggin and Egf were omitted from the culture medium to select for *Apc* and *Kras* mutant organoids respectively. After selection, single organoids were manually picked for clonal expansion and then genotyped. Genomic DNA was isolated using the DNA micro kit (Qiagen) according to the manufacturer's instructions and PCR amplification was performed using the GoTaq Flexi DNA polymerase kit (Promega). Organoid genotype was confirmed by Sanger sequencing. Primers are listed in **Table S5.**

### Protein extraction and Western blotting

Organoids were harvested three days after splitting and washed in cold PBS and collected in cell recovery solution (Corning) according to the manufacturer's instructions. Whole cell lysates were obtained by direct lysis in RIPA buffer (50 mM Tris- HCl pH 8.0, 150 mM NaCl, 0.1% SDS, 0.5% Na-Deoxycholate, 1% NP-40)

containing complete protease inhibitors (Sigma-Aldrich) for 30 minutes on ice. Proteins were run on SDS–PAGE gels and transferred to PVDF membranes, followed by blocking with Odyssey blocking buffer (LI-COR). The antibodies used are described in **Table S6**. Blots were imaged with the Amersham Typhoon (GE Healthcare Life Sciences).

**Immunofluorescence**

Organoids were seeded in 15-well Ibidi chambers after passaging and fixed 3-4 days later in 4% Paraformaldehyde (Sigma-Aldrich) for 60 minutes at room temperature. After fixation organoids were washed with cold PBS and permeabilized with PBD0.2T (48,5 mL PBS, 1 mL 10%Triton, 0,5mL DMSO and 0,5 g BSA) for 20 minutes at room temperature, after which they were incubated with primary antibodies diluted in PBD0.2T buffer at 4°C overnight. Washes were performed PBD0.2T buffer and secondary antibodies incubated 2-3 hours at room temperature. All antibodies are described in **Table S7**. Quantification of the nuclear fraction of Yap was analyzed using the JACoP Fiji plugin. EdU incorporation assays were performed by culturing organoids in ENR medium containing 10 µM Edu for 6 hours to cells, after which single organoids were harvested, fixed in 4% PFA and EdU-labeling was performed according to manufacturer instructions (Click-iT EdU Cell Proliferation Kit for Imaging, Thermo Fisher). Images were acquired with a Zeiss LSM700 or LSM880 confocal microscope.

**Patient tissue samples and counting**

Patient material was collected from the pathology archives of Dutch hospitals (UMC). In total five PJS patients were included in this study. Five normal controls were randomly selected. In 10 microscopically normal looking crypts $MUC2^+$ cells were counted from the bottom toward to the top of the crypt. Only longitudinally oriented crypts that were completely visible on the slide, were counted. Cell positions were defined as the bottom of the crypt is cell position one (1), going upward to cell position +2, +3, and so forth till cell position 30. Within the part of the crypt between cell position 1 and 30, the number of positively labelled cells were counted. Also, the total cell position was determined by adding up each cell position of a labelled cell and average cell position of the labelled cells was determined by adding up each cell position of a labelled cell and dividing the sum by the total number of labelled cells counted.

**Immunohistochemistry**

Fresh mouse small intestinal organoids were fixed in 4% Formaldehyde three days after splitting for 1 hour followed by dehydration in 25%, 50% and 70% ethanol and embedding in paraffin. Briefly, 4µm FFPE organoid or PJS patient tissue sections were obtained, deparaffinized, blocked in 0.3% H2O2 in methanol for 20 minutes. Antigen retrieval was performed in Tris/EDTA buffer (10 mM/1 mM; pH 9.0) or Sodium-citrate buffer (0,01 M/pH6.0) for 20 minutes at 100°C. Nonspecific binding sites were blocked using Protein Block Serum free (DAKO) for 10 minutes, followed by primary antibody incubation. Antibody binding was visualized using the using BrightVision Goat anti Rabbit / Poly-AP and BrightVision Goat anti Mouse / Poly-HRP (VWR/ImmunoLogic), with DAB as chromogen (Sigma-Aldrich). Sections were counterstained with Haematoxylin or neutral red and mounted using Pertex. Primary antibodies are described in **Table S8**.

**Electron microscopy**

Three days after splitting, organoids were fixed in a solution of 2% paraformaldehyde and 2.5% glutaraldehyde in 0.1 M phosphate buffer (pH 7.4) overnight at 4°C. On the following day, organoids were washed twice in 0.1 M phosphate buffer (pH 7.4) and subsequently post-fixed with 1% Osmium tetroxide for 2 hours at 4°C. Organoids were then stained with 0.5% uranyl acetate 1 hour at 4°C in the dark. Matrigel droplets were transferred into glass vials for dehydration with increasing acetone concentrations according to the following protocol: 70% overnight at 4°C, 90% for 15 minutes at RT, 96% for 15 minutes at RT, and 100% 3 times for 30 minutes each at RT. After dehydration, samples were embedded in EPON resin. Ultrathin sections of 65 nm were obtained with a Leica UC7 microtome and stained with uranyl and lead citrate. Electron microscopy was performed in the Cell Microscopy Core (CMC) of the UMC Utrecht. Sections were imaged with a JEOL JEM-1010 transmission electron microscope (TEM).

**Cell viability assay**

For the organoid reconstitution assays, organoids were dissociated to single cells after incubation with TrypLE (Life Technologies) for 5 min at 37°C. Dissociated organoids were passed through a 40 µm strainer and counted. Cells were seeded at a density of 5000 cells/10µl Matrigel and cultured in ENR medium with 10 µM Y-27632 (Sigma-Aldrich) for 7 days. Organoids were then lysed with CellTiter-Glo® (Promega) according to the manufacturer's protocol. ATP produced by viable cells was measured by a Berthold luminometer Centro LB960.

**Bulk RNA sequencing and data analysis**

Organoids were lysed in RLT lysis buffer (Qiagen) 3-5 days after passaging. Biological triplicates were employed. RNA was obtained using the Qiagen QiaSymphony SP (Qiagen) according to the manufacturer's protocol. Single-end RNASeq reads were processed using the UMCU RNASeq pipeline (https://github.com/UMCUGenetics/RNASeq, v2.3.0) with default settings. Read quality was assessed by FastQC (0.11.4) followed by splice-aware alignment against the mouse reference genome (GRCm38) with STAR (2.4.2a). RNA expression quantification was performed with htseq-count (0.6.0) in reverse-stranded mode. Differential gene expression analysis was performed with the DESeq2 (1.22.2) R package. In each comparison, genes were selected with an absolute fold-change > 2 and alpha P > 0.05. Data clustering and generation of heatmaps was performed with pheatmap. Gene Set Enrichment Analysis was performed using GSEA (v4.2.0, Windows App) and visualized using ggplot2. Intestinal cell-type specific gene sets for GSEA were obtained from Extended Figure Table 3 of Haber et al., 2017 (Haber *et al.*, 2017). The other datasets employed in GSEA were derived from previously published studies (Mustata *et al.*, 2013; Gregorieff *et al.*, 2015; Nusse *et al.*, 2018; Yui, Azzolin, Maimets, Pedersen, Fordham, Hansen, Larsen, Guiu, M. R. P. P. Alves, *et al.*, 2018; Ayyaz *et al.*, 2019; Chen *et al.*, 2021; Qu *et al.*, 2021; Joanito *et al.*, 2022). Human gene sets were converted to their respective mouse homologs using biomaRt (2.50.3) in R where necessary.

**Single cell RNA sequencing**

*Sample preparation and sequencing:* Single cells from organoid were harvested using TrypLE incubation at 37 °C, four days after passaging. Cells were filtered through a 40 µm nylon cell strainer (Falcon). scRNA-seq

was performed according to the Sort-seq protocol (Muraro *et al.*, 2016). Libraries were sequenced on an Illumina NextSeq500 at paired-end 60- and 26-bp read length and 75,000 reads per cell.

*Mapping and filtering*: The Sharq pipeline was used to process the sequencing data (Candelli *et al.*, 2018). Mapping was performed using STAR (version 2.6.1), on the Genome Reference Consortium Mouse built 38 (GRCm38). Read assignment was with feature Counts version 1.5.2 using a gene annotation based on GENCODE version M14.

External RNA controls (ERCCS) and transcripts mapping to the mitochondrial genome were removed from all cells. Low quality cell barcodes having either less than 800 unique transcripts, 200 genes 33.3% mitochondrial transcripts or over 4-fold non-exonic to exonic reads were excluded, as well as barcodes with over 100,000 unique transcripts.

*scRNA-seq analysis*: Unique transcript counts were normalized using sctransform (Hafemeister and Satija, 2019) and analyzed using the Seurat R package (version 4.1.0) (Butler *et al.*, 2018). From the top 3000 variable genes, genes associated with cell cycle phase, dissociation stress (heat shock and chaperone proteins according to GO:0006986), sex (Xist, Tsix, and Y chromosome-specific genes), and activity (ribosomal protein genes according to GO:0022626) were removed from the list of variable genes to avoid biases in cell clustering, as described before (Hanemaaijer *et al.*, 2021). The first 20 principal components were used both to calculate dimensionality reduction using UMAP and to perform clustering with a resolution of 1, k.param = 10 and the Louvain algorithm.

**TCGA data analysis**

*STK11/LKB1* co-occurring mutations were determined using cBioPortal (https://www.cbioportal.org/). All bowel datasets were selected and using the comparison tool co-occuring genomic alterations were identified in *STK11/LKB1* WT and *STK11/LKB1* mutant samples. Signature scores for a *Lkb1*-deficient geneset were calculated for each sample as log2 Z-score over the samples from the TCGA Colon Adenocarcinoma (2022 – v32) set using the R2 genomic analysis platform (http://r2.amc.nl). The *Lkb1*-deficient signature was determined as genes that were significantly (padj < 0.05) upregulated in all comparisons (WT vs. *Lkb1*$^{+/-}$, WT vs. *Lkb1*$^{bud\ -/-}$, WT vs. *Lkb1*$^{cys\ -/-}$).

## Supplementary information

**Table S4: gRNA sequences**

| Gene | Sequence |
|---|---|
| *Lkb1* gRNA1 | AGCTTGGCGCGTTTGCGGCG |
| *Lkb1* gRNA2 | TGAGGATCTTGACCGCCCTG |
| Apc | TGTCTGGCTCCGGTAAGTGA |
| Kras | CTTGTGGTGGTTGGAGCTGG |

**Table S5: Genotyping primers**

| Gene | Forward primer | Reverse Primer |
|---|---|---|
| *Lkb1* gRNA1 | GGGGAAAATCAAAAGTGAAGAA | CCCTCTAGCTGCGTAAACAAAC |
| *Lkb1* gRNA2 | CTCCACCGAGGTAATCTACCAGCCG | TCTAACCGTTTTCTCTTCTCATTTCC |
| *Apc* | ATAGAAACAGCACTGACCCAAATTTCA | AGGCCTCTTTGCTTAGAGCTTTCATAA |
| *Kras* | TGGCTCCAACACAGATGTTC | GGATGGCATCTTGGACCTTA |

**Table S6: Western Blot antibodies**

| Antibody | Dilution | Supplier | Cat. number |
|---|---|---|---|
| Anti-LKB1 | 1:1000 | Santa Cruz | sc-32245 |
| Anti-GAPDH | 1:8000 | Millipore | CB1001 |
| Anti-mouse Alexa 800 | 1:5000 | LI-COR | 926-32211 |
| Anti-rabbit Alexa 680 | 1:5000 | LI-COR | 925-68070 |

**Table S7: Immunostaining antibodies**

| Antibody | Dilution | Supplier | Cat. number |
|---|---|---|---|
| Anti-Muc2 | 1:200 (IF)<br>1:1000 (IHC) | Santa Cruz | sc-515032 |
| Anti-Lysozyme1 | 1:200 (IF)<br>1:2000 (IHC) | Dako | A0099 |
| Anti-ANXA1 | 1:200 (IF)<br>1:1000 (IHC) | Atlas Antibodies | HPA011271 |
| Anti-YAP | 1:200 (IF) | Santa Cruz | sc-101199 |
| Anti-Cleasved-Caspase-3 | 1:200 (IF) | Cell Signalling | 9661 |
| Anti-rabbit Alexa Fluor 488 | 1:300 (IF) | Invitrogen | A11034 |
| Anti-mouse Alexa 488 | 1:300 (IF) | Invitrogen | A11029 |
| DAPI | 1:1000 (IF) | Sigma | D9542 |
| Click-iT™ EdU Alexa Fluor™ 647 | n.a. | Invitrogen | C10424 |

| | | | |
|---|---|---|---|
| Alexa Fluor™ 647 Phalloidin | 1:500 (IF) | Invitrogen | A22287 |

## Data availability

The scRNA-seq and bulk RNA-seq data generated in this study will be uploaded to Gene Expression Omnibus (GEO) upon publication. If needed earlier, data can be requested via the corresponding author.

## Author contributions

S.F.P, H.M., A.M. and M.M.M., conceived and designed the experiments. S.F.P, H.M., A.M., D.X., F.H.M.M., C.J. and A.R.K performed the experiments. S.F.P, H.M., A.M., J.Y.V., J.S., T.M., T.C., R.S., J.R., F.C.P.H., G.J.A.O. and M.M.M. analyzed the data. W.W.J.L. and G.J.A.O. provided patient material. S.F.P, H.M., A.M., J.Y.V. and M.M.M. wrote the manuscript, which was reviewed by all authors.

## Disclosure and competing interest statement

M.M.M. is co-founder and shareholder of Laigo Bio and inventor on patents related to membrane protein degradation; J.R. is co-founder of Cyclomics BV., a genomics company.

## Acknowledgements

The authors thank members of the Maurice laboratory for helpful discussions and suggestions. PiggyBac Transposase and pPB-CAG-rtTA_Hygromycin were a kind gift from B.K. Koo. This work is part of the Oncode Institute, which is partly financed by the Dutch Cancer Society. This work was supported by the China Scholarship Council (to H.M.), the Dutch Cancer Society KWF Grant 13112 (to M.M.M.), Zon-MW TOP grant 91218050 (to M.M.M.) and NWO Gravitation project IMAGINE! (to M.M.M.).

**Figure 1**

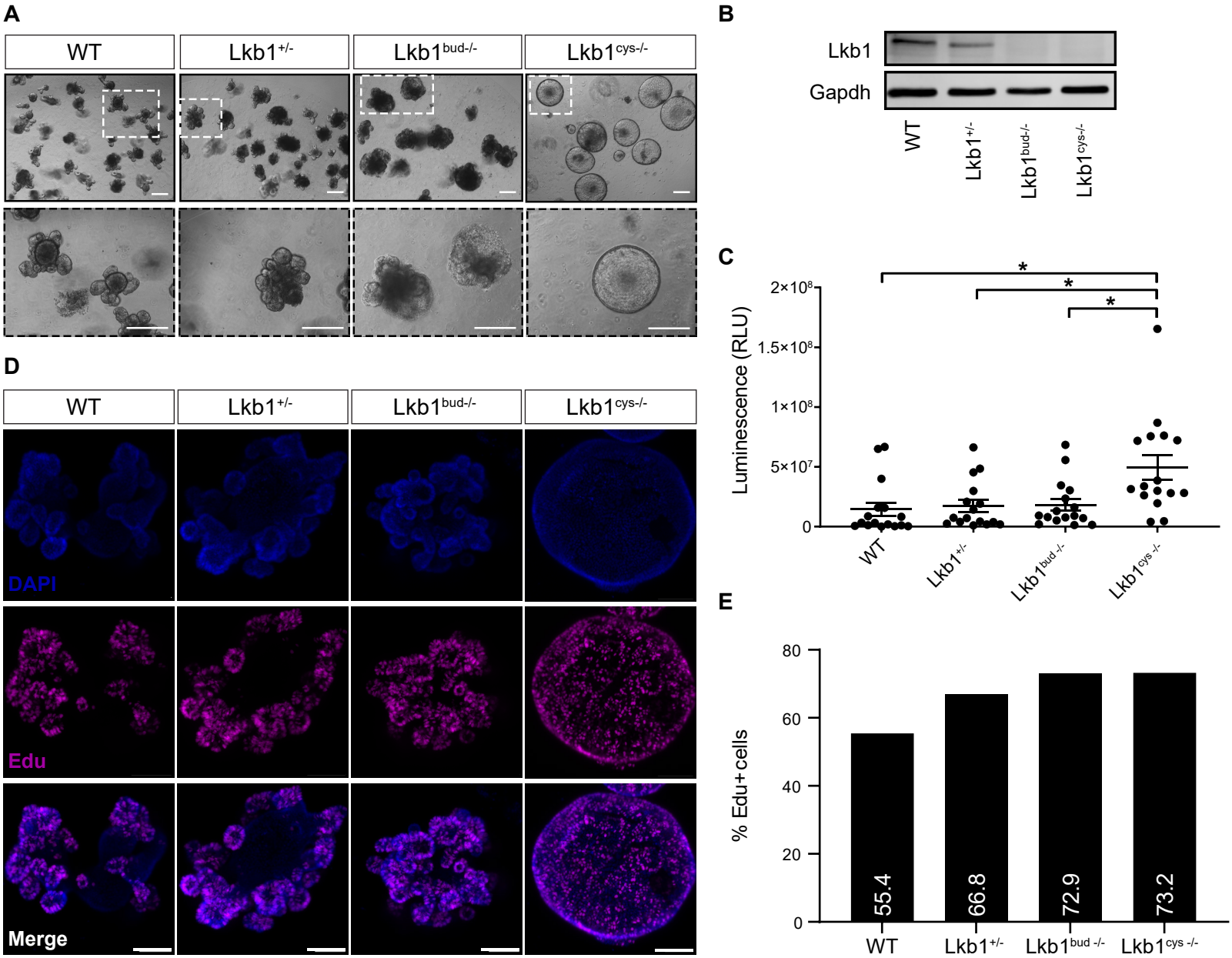
A
WT
Lkb1+/-
Lkb1bud-/-
Lkb1cys-/-
B
Lkb1
Gapdh
WT
Lkb1+/-
Lkb1bud-/-
Lkb1cys-/-
C
Luminescence (RLU)
2×10^8
1.5×10^8
1×10^8
5×10^7
0
*
*
*
WT
Lkb1+/-
Lkb1bud -/-
Lkb1cys -/-
D
WT
Lkb1+/-
Lkb1bud-/-
Lkb1cys-/-
DAPI
Edu
Merge
E
% Edu+cells
80
60
40
20
0
55.4
66.8
72.9
73.2
WT
Lkb1+/-
Lkb1bud -/-
Lkb1cys -/-

**Figure 2**

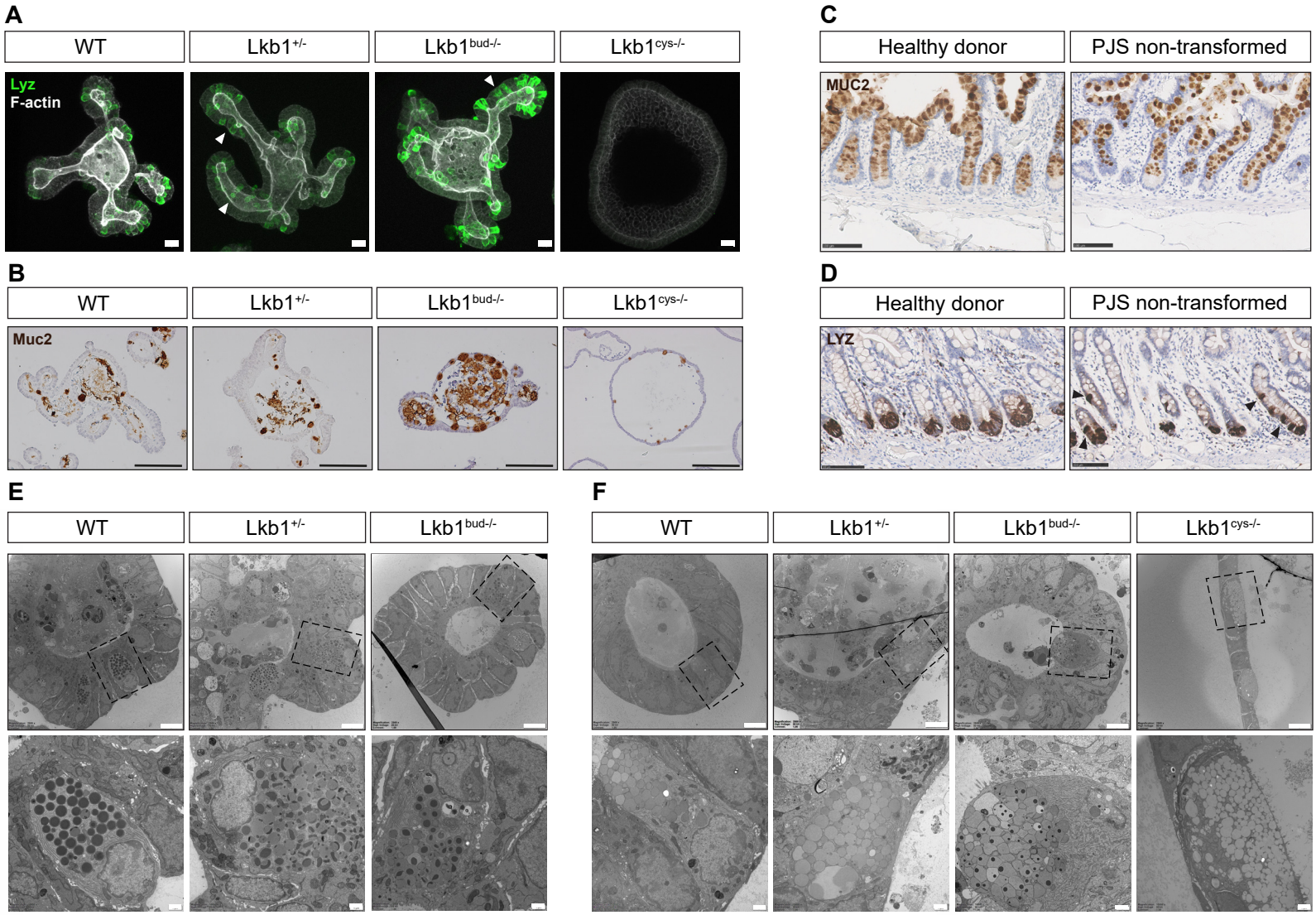
A
WT
Lkb1+/-
Lkb1bud-/-
Lkb1cys-/-
Lyz
F-actin
B
WT
Lkb1+/-
Lkb1bud-/-
Lkb1cys-/-
Muc2
C
Healthy donor
PJS non-transformed
MUC2
D
Healthy donor
PJS non-transformed
LYZ
E
WT
Lkb1+/-
Lkb1bud-/-
F
WT
Lkb1+/-
Lkb1bud-/-
Lkb1cys-/-

**Figure 3**

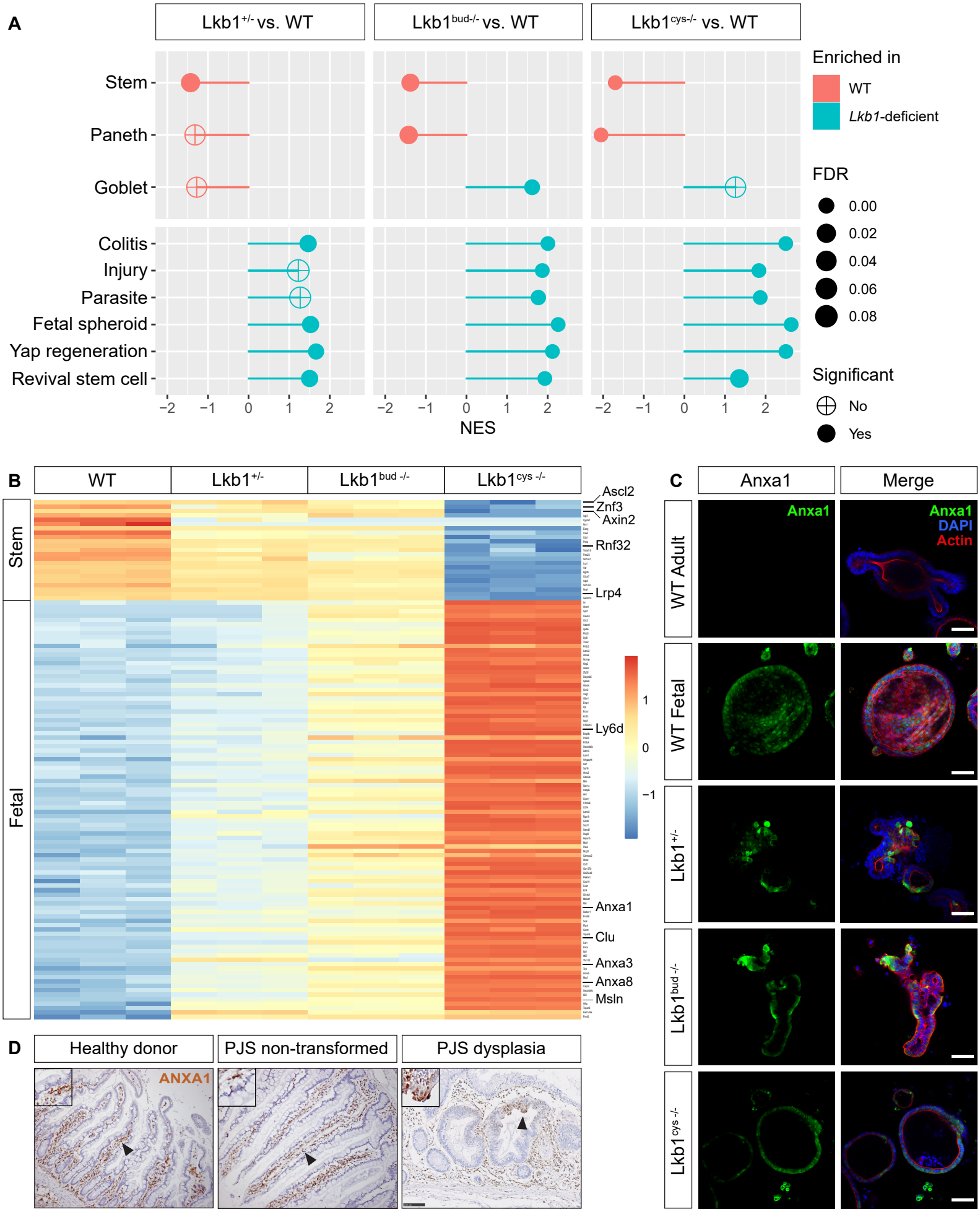
A
Lkb1+/- vs. WT
Lkb1bud-/- vs. WT
Lkb1cys-/- vs. WT
Stem
Paneth
Goblet
Colitis
Injury
Parasite
Fetal spheroid
Yap regeneration
Revival stem cell
−2 −1 0 1 2
NES
Enriched in
WT
Lkb1-deficient
FDR
0.00
0.02
0.04
0.06
0.08
Significant
No
Yes
B
WT
Lkb1+/-
Lkb1bud -/-
Lkb1cys -/-
Stem
Fetal
Ascl2
Znf3
Axin2
Rnf32
Lrp4
Ly6d
Anxa1
Clu
Anxa3
Anxa8
Msln
1
0
−1
C
Anxa1
Merge
WT Adult
WT Fetal
Lkb1+/-
Lkb1bud -/-
Lkb1cys -/-
Anxa1
Anxa1
DAPI
Actin
D
Healthy donor
PJS non-transformed
PJS dysplasia
ANXA1

**Figure 4**

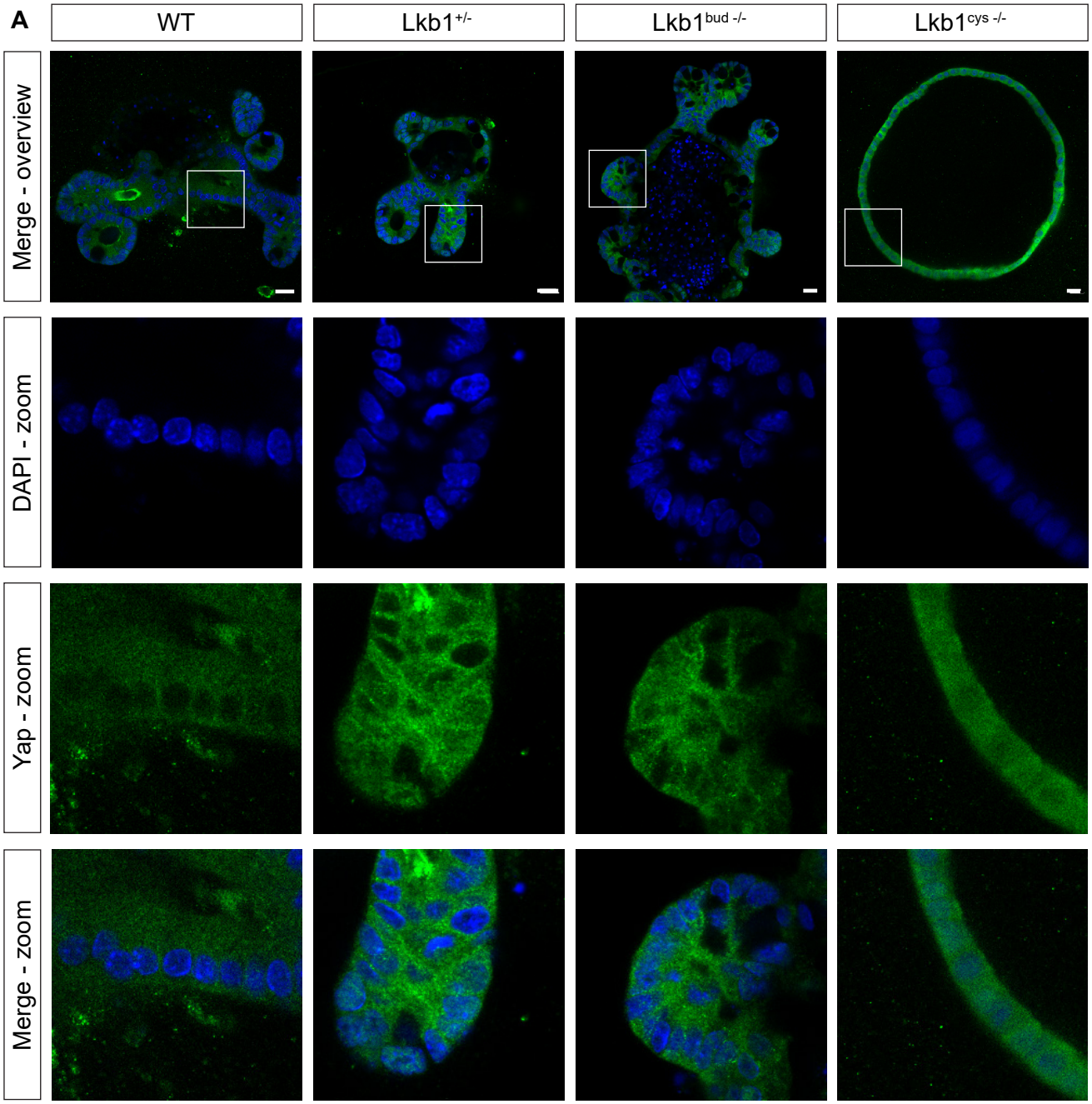
A
WT
Lkb1+/-
Lkb1bud -/-
Lkb1cys -/-
Merge - overview
DAPI - zoom
Yap - zoom
Merge - zoom

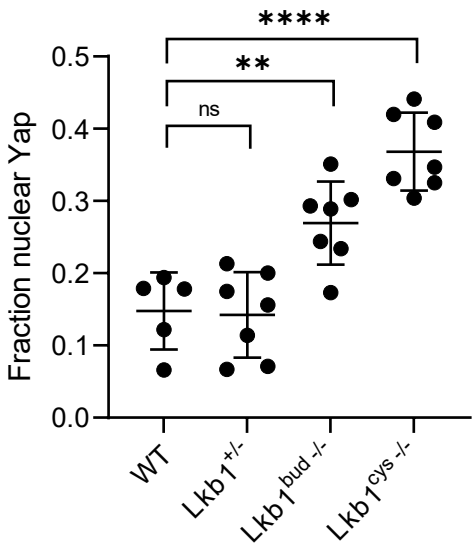
B
****
**
ns
Fraction nuclear Yap
0.0
0.1
0.2
0.3
0.4
0.5
WT
Lkb1+/-
Lkb1bud -/-
Lkb1cys -/-

**Figure 5**

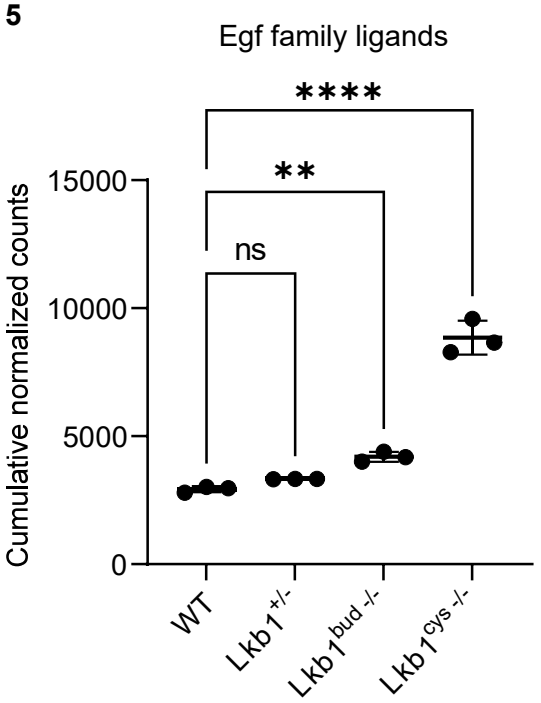
A
Egf family ligands
****
**
ns
15000
10000
5000
0
Cumulative normalized counts
WT
Lkb1+/-
Lkb1bud -/-
Lkb1cys -/-

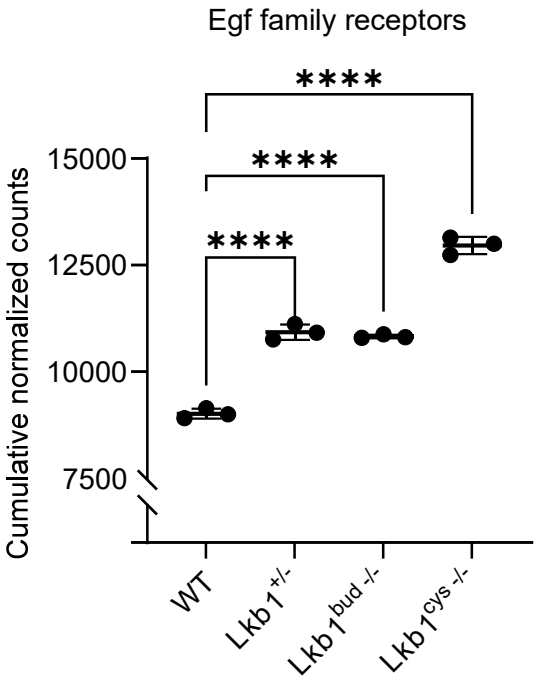
B
Egf family receptors
****
****
****
15000
12500
10000
7500
Cumulative normalized counts
WT
Lkb1+/-
Lkb1bud -/-
Lkb1cys -/-

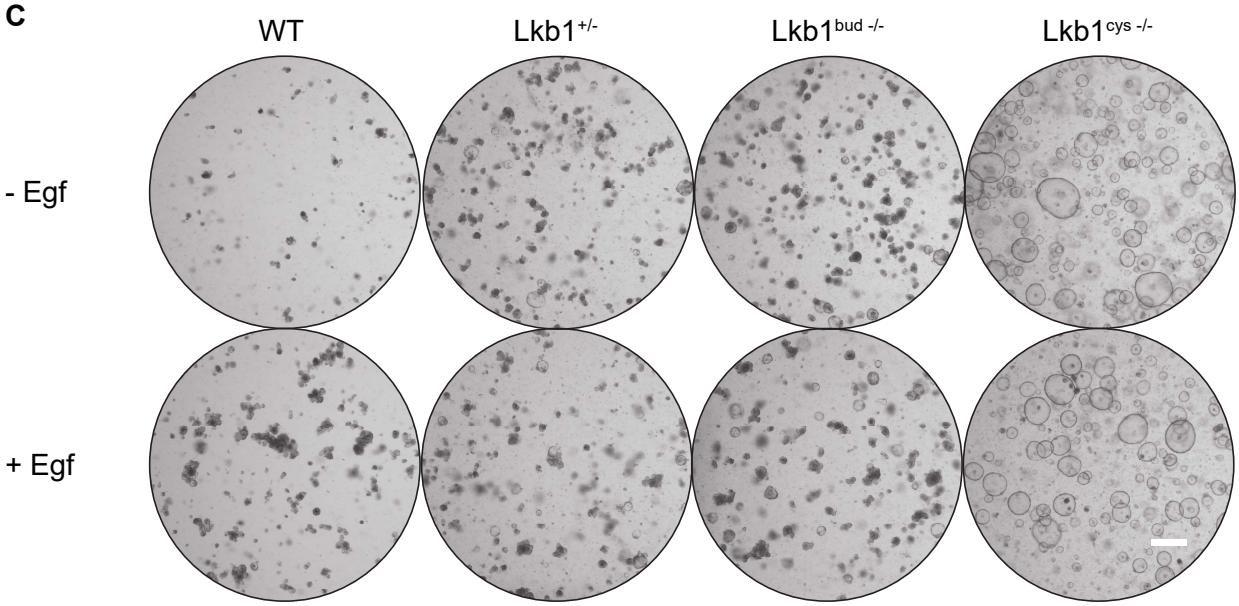
C
WT
Lkb1+/-
Lkb1bud -/-
Lkb1cys -/-
- Egf
+ Egf

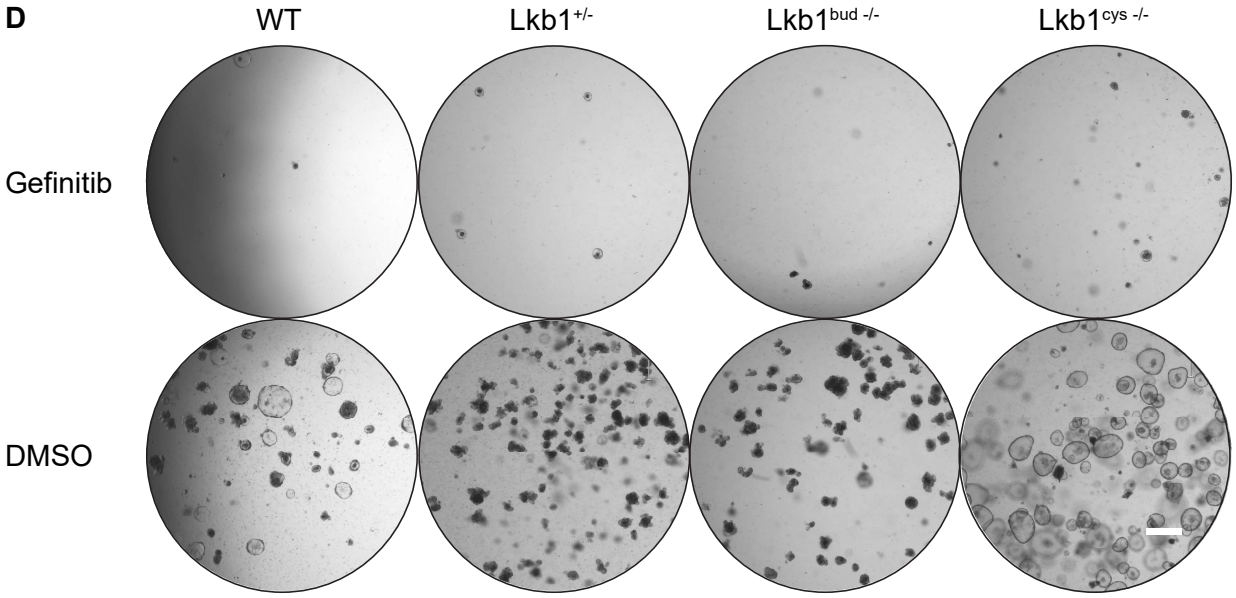
D
WT
Lkb1+/-
Lkb1bud -/-
Lkb1cys -/-
Gefinitib
DMSO

**Figure 6**

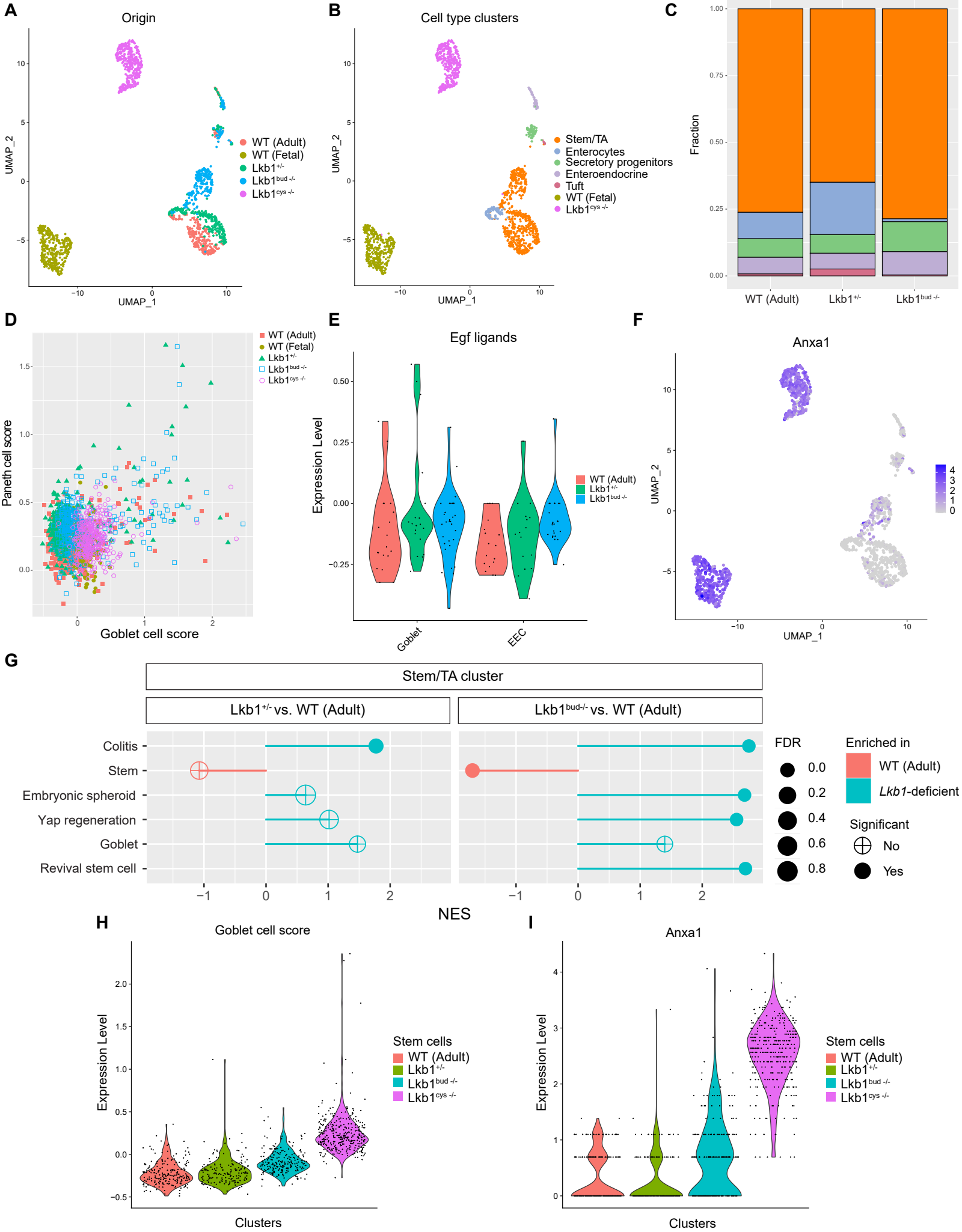
A
Origin
UMAP_2
UMAP_1
WT (Adult)
WT (Fetal)
Lkb1+/-
Lkb1bud -/-
Lkb1cys -/-
B
Cell type clusters
Stem/TA
Enterocytes
Secretory progenitors
Enteroendocrine
Tuft
WT (Fetal)
Lkb1cys -/-
C
Fraction
WT (Adult)
Lkb1+/-
Lkb1bud -/-
D
Paneth cell score
Goblet cell score
E
Egf ligands
Expression Level
Goblet
EEC
F
Anxa1
G
Stem/TA cluster
Lkb1+/- vs. WT (Adult)
Lkb1bud-/- vs. WT (Adult)
Colitis
Stem
Embryonic spheroid
Yap regeneration
Goblet
Revival stem cell
NES
FDR
Enriched in
WT (Adult)
Lkb1-deficient
Significant
No
Yes
H
Goblet cell score
Stem cells
Clusters
I
Anxa1

## Figure 7

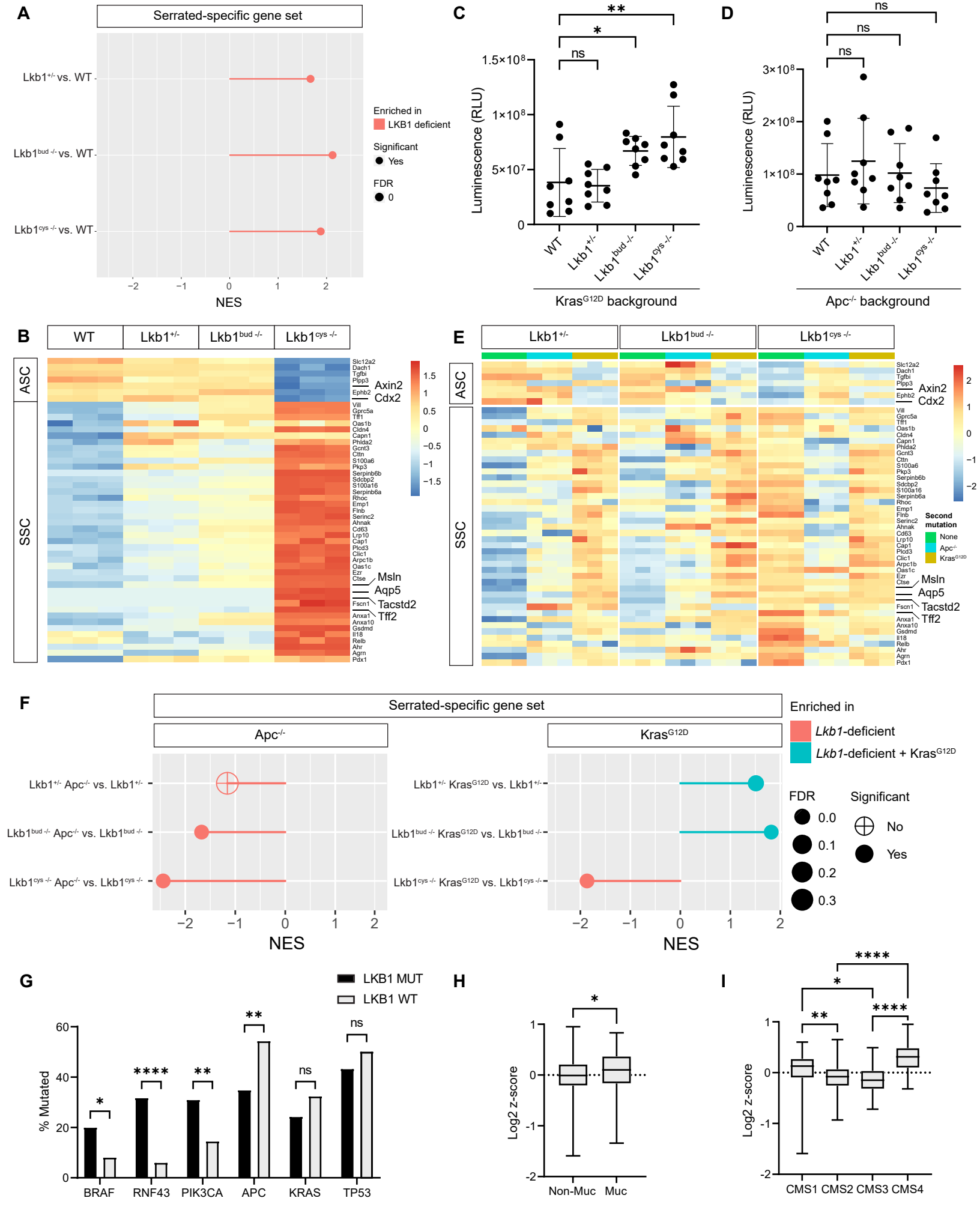
A
Serrated-specific gene set
Lkb1+/- vs. WT
Lkb1bud -/- vs. WT
Lkb1cys -/- vs. WT
NES
Enriched in
LKB1 deficient
Significant
Yes
FDR
0
C
Luminescence (RLU)
WT
Lkb1+/-
Lkb1bud -/-
Lkb1cys -/-
KrasG12D background
D
Apc-/- background
B
WT
Lkb1+/-
Lkb1bud -/-
Lkb1cys -/-
ASC
SSC
Axin2
Cdx2
Msln
Aqp5
Tacstd2
Tff2
E
Second mutation
None
Apc-/-
KrasG12D
F
Serrated-specific gene set
Apc-/-
KrasG12D
Lkb1+/- Apc-/- vs. Lkb1+/-
Lkb1bud -/- Apc-/- vs. Lkb1bud -/-
Lkb1cys -/- Apc-/- vs. Lkb1cys -/-
Lkb1+/- KrasG12D vs. Lkb1+/-
Lkb1bud -/- KrasG12D vs. Lkb1bud -/-
Lkb1cys -/- KrasG12D vs. Lkb1cys -/-
Enriched in
Lkb1-deficient
Lkb1-deficient + KrasG12D
FDR
Significant
No
Yes
G
LKB1 MUT
LKB1 WT
% Mutated
BRAF
RNF43
PIK3CA
APC
KRAS
TP53
H
Log2 z-score
Non-Muc
Muc
I
CMS1
CMS2
CMS3
CMS4

# Figure S1

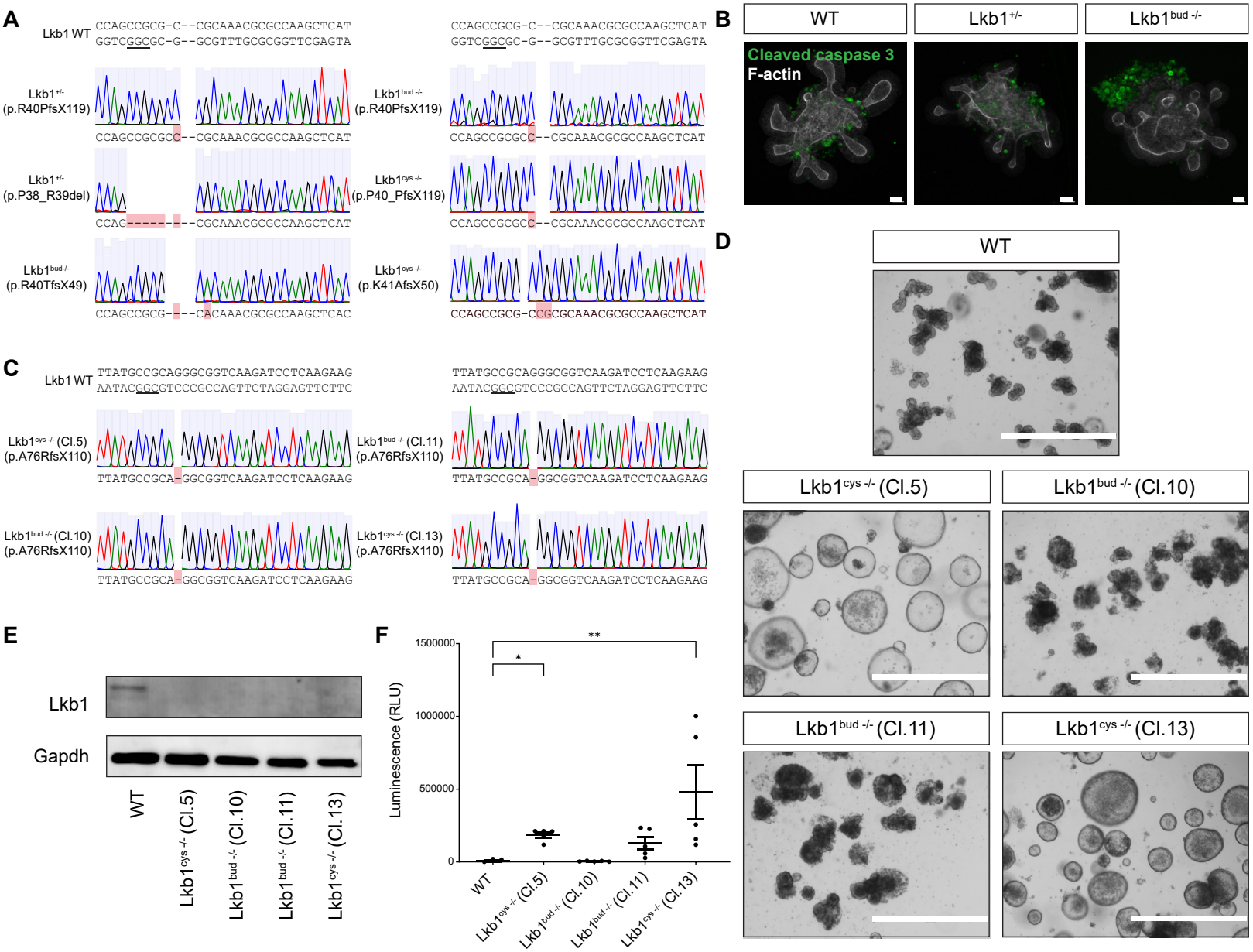
A
Lkb1 WT
CCAGCCGCG-C--CGCAAACGCGCCAAGCTCAT
GGTCGGCGC-G--GCGTTTGCGCGGTTCGAGTA
CCAGCCGCG-C--CGCAAACGCGCCAAGCTCAT
GGTCGGCGC-G--GCGTTTGCGCGGTTCGAGTA
Lkb1+/- (p.R40PfsX119)
CCAGCCGCGCC--CGCAAACGCGCCAAGCTCAT
Lkb1bud -/- (p.R40PfsX119)
CCAGCCGCGCC--CGCAAACGCGCCAAGCTCAT
Lkb1+/- (p.P38_R39del)
CCAG-------CGCAAACGCGCCAAGCTCAT
Lkb1cys -/- (p.P40_PfsX119)
CCAGCCGCGCC--CGCAAACGCGCCAAGCTCAT
Lkb1bud-/- (p.R40TfsX49)
CCAGCCGCG---CACAAACGCGCCAAGCTCAC
Lkb1cys -/- (p.K41AfsX50)
CCAGCCGCG-CCGCGCAAACGCGCCAAGCTCAT
B
WT
Lkb1+/-
Lkb1bud -/-
Cleaved caspase 3
F-actin
C
Lkb1 WT
TTATGCCGCAGGGCGGTCAAGATCCTCAAGAAG
AATACGGCGTCCCGCCAGTTCTAGGAGTTCTTC
TTATGCCGCAGGGCGGTCAAGATCCTCAAGAAG
AATACGGCGTCCCGCCAGTTCTAGGAGTTCTTC
Lkb1cys -/- (Cl.5) (p.A76RfsX110)
TTATGCCGCA-GGCGGTCAAGATCCTCAAGAAG
Lkb1bud -/- (Cl.11) (p.A76RfsX110)
TTATGCCGCA-GGCGGTCAAGATCCTCAAGAAG
Lkb1bud -/- (Cl.10) (p.A76RfsX110)
TTATGCCGCA-GGCGGTCAAGATCCTCAAGAAG
Lkb1cys -/- (Cl.13) (p.A76RfsX110)
TTATGCCGCA-GGCGGTCAAGATCCTCAAGAAG
D
WT
Lkb1cys -/- (Cl.5)
Lkb1bud -/- (Cl.10)
Lkb1bud -/- (Cl.11)
Lkb1cys -/- (Cl.13)
E
Lkb1
Gapdh
WT
Lkb1cys -/- (Cl.5)
Lkb1bud -/- (Cl.10)
Lkb1bud -/- (Cl.11)
Lkb1cys -/- (Cl.13)
F
Luminescence (RLU)
1500000
1000000
500000
0
*
**
WT
Lkb1cys -/- (Cl.5)
Lkb1bud -/- (Cl.10)
Lkb1bud -/- (Cl.11)
Lkb1cys -/- (Cl.13)

**Figure S2**

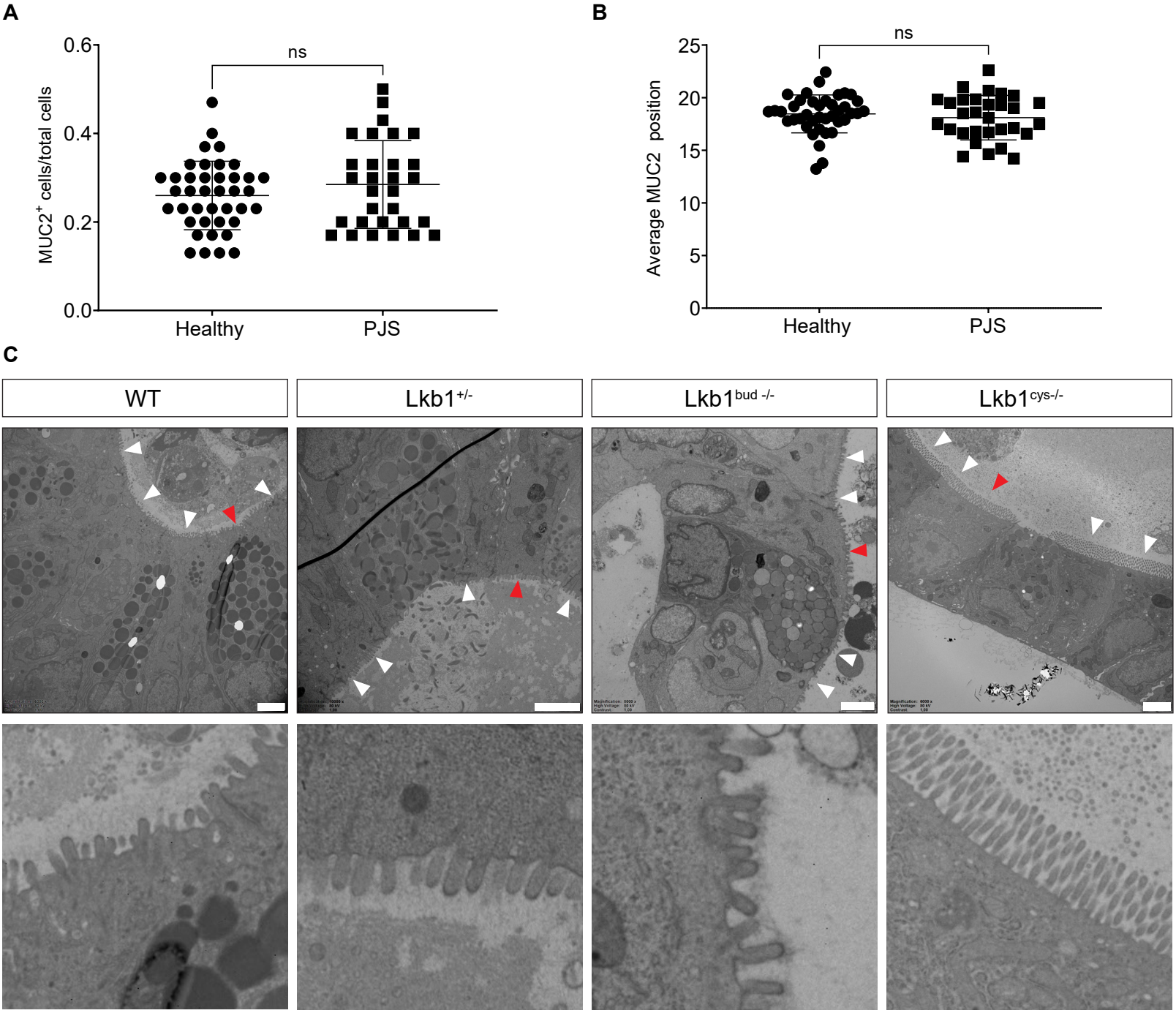
A
0.6
0.4
0.2
0.0
MUC2+ cells/total cells
ns
Healthy
PJS
B
25
20
15
10
5
0
Average MUC2 position
ns
Healthy
PJS
C
WT
Lkb1+/-
Lkb1bud -/-
Lkb1cys-/-

**Figure S3**

**A**

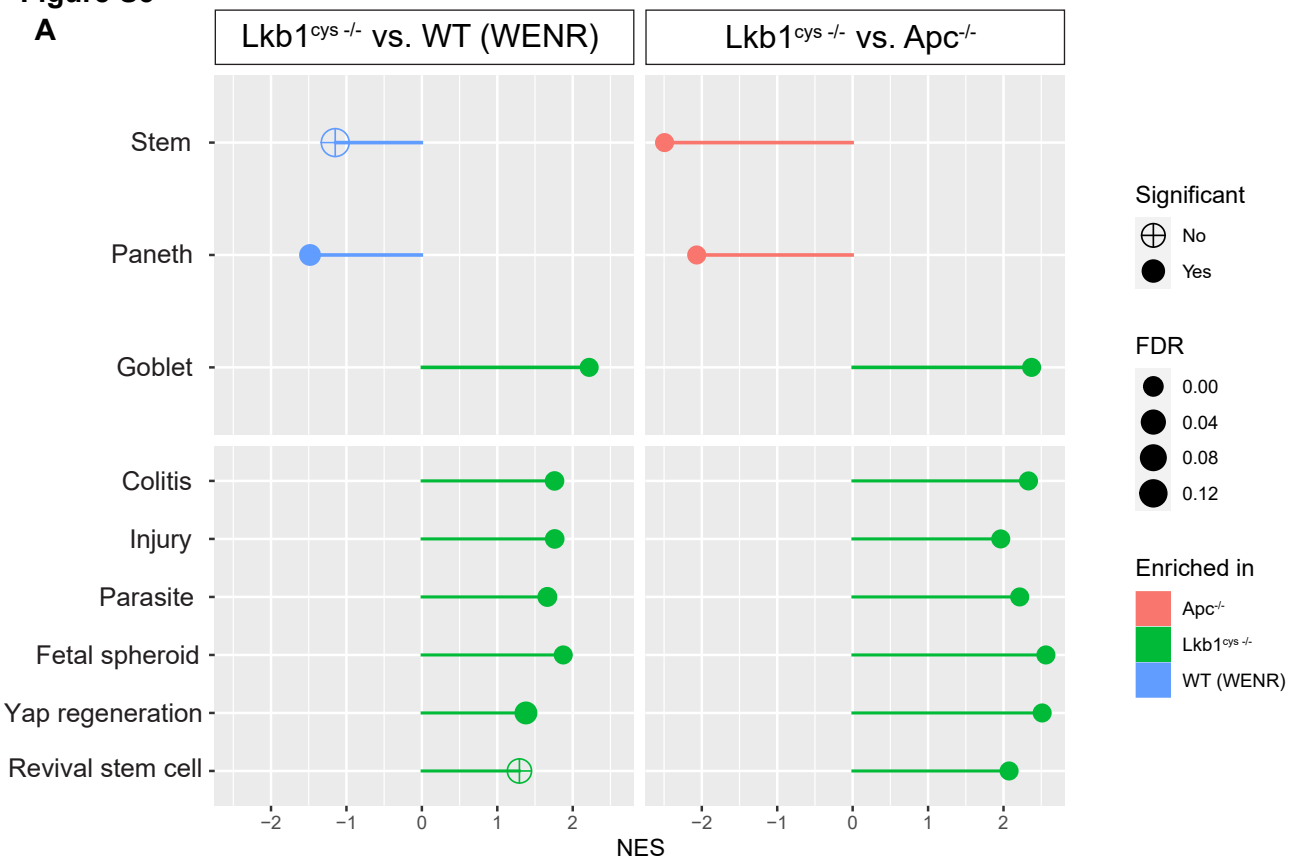
Lkb1cys -/- vs. WT (WENR)
Lkb1cys -/- vs. Apc-/-
Stem
Paneth
Goblet
Colitis
Injury
Parasite
Fetal spheroid
Yap regeneration
Revival stem cell
−2
−1
0
1
2
NES
Significant
No
Yes
FDR
0.00
0.04
0.08
0.12
Enriched in
Apc-/-
Lkb1cys -/-
WT (WENR)

**B**

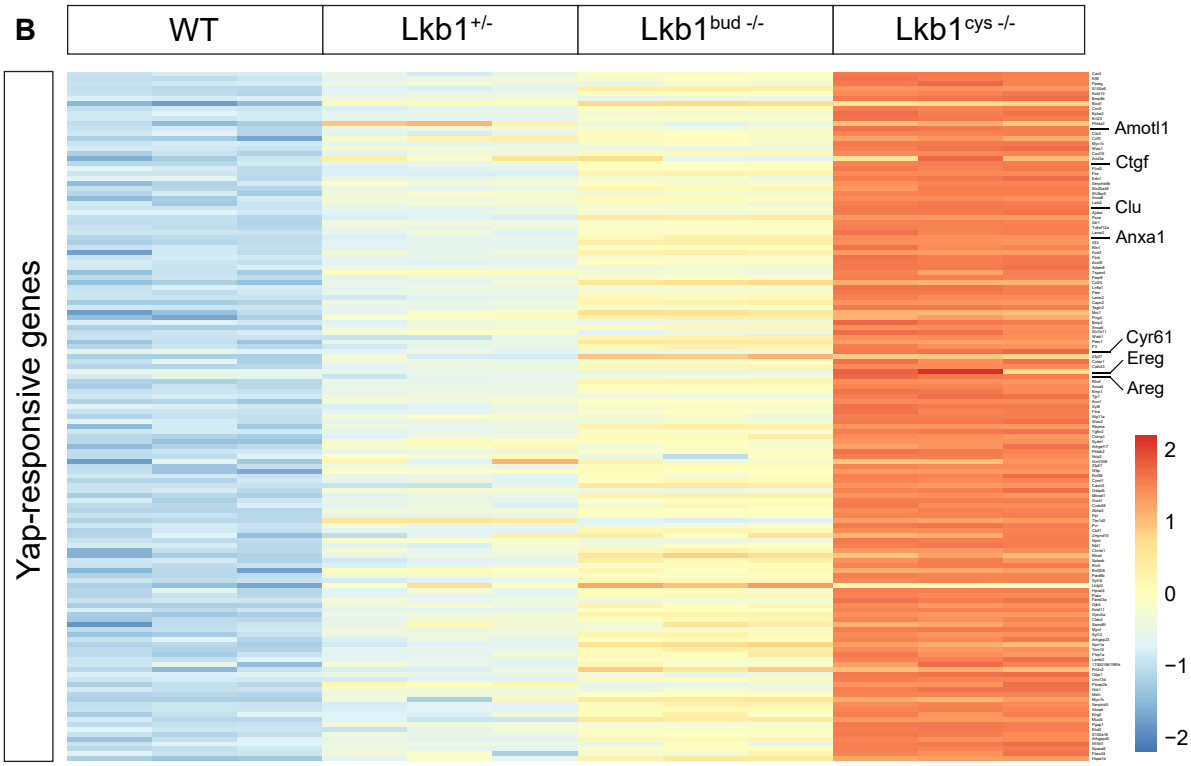
WT
Lkb1+/-
Lkb1bud -/-
Lkb1cys -/-
Yap-responsive genes
Amotl1
Ctgf
Clu
Anxa1
Cyr61
Ereg
Areg
2
1
0
−1
−2

**Figure S4**

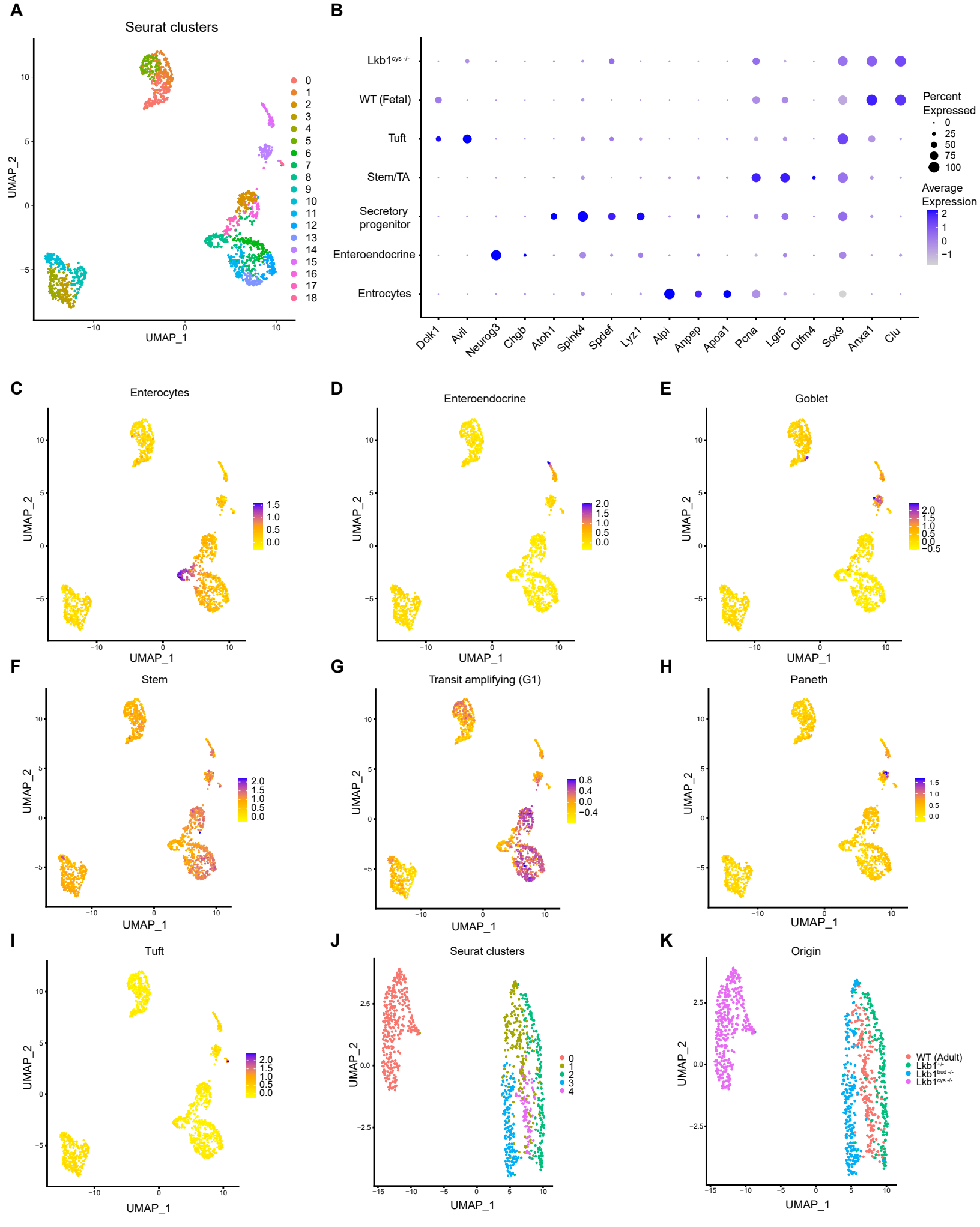
A
Seurat clusters
UMAP_2
UMAP_1
0
1
2
3
4
5
6
7
8
9
10
11
12
13
14
15
16
17
18
B
Lkb1cys -/-
WT (Fetal)
Tuft
Stem/TA
Secretory progenitor
Enteroendocrine
Entrocytes
Dclk1
Avil
Neurog3
Chgb
Atoh1
Spink4
Spdef
Lyz1
Alpi
Anpep
Apoa1
Pcna
Lgr5
Olfm4
Sox9
Anxa1
Clu
Percent Expressed
0
25
50
75
100
Average Expression
2
1
0
−1
C
Enterocytes
D
Enteroendocrine
E
Goblet
F
Stem
G
Transit amplifying (G1)
H
Paneth
I
Tuft
J
Seurat clusters
K
Origin
WT (Adult)
Lkb1+/-
Lkb1bud -/-
Lkb1cys -/-

**Figure S5**

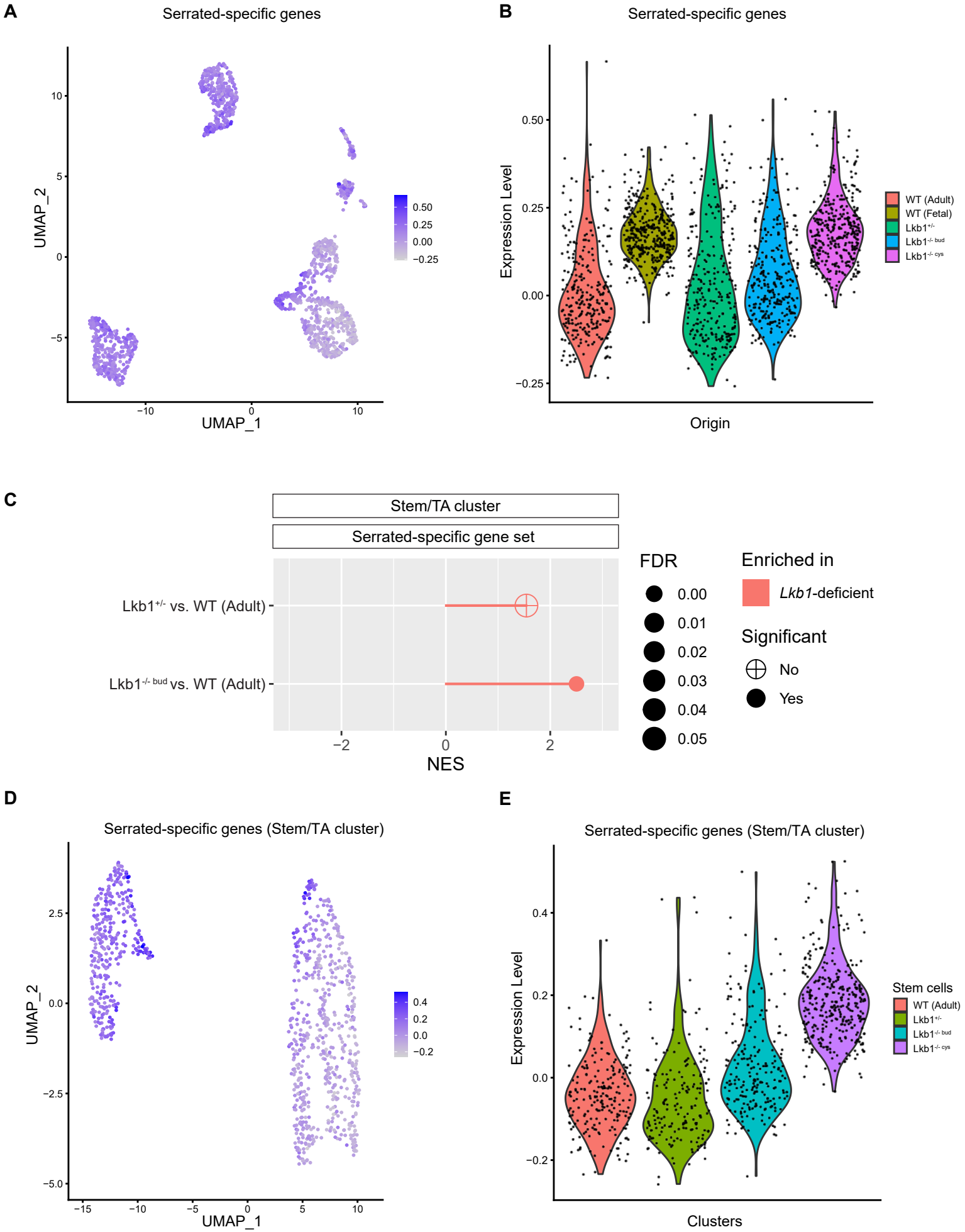
A
Serrated-specific genes
UMAP_2
UMAP_1
0.50
0.25
0.00
−0.25
B
Serrated-specific genes
Expression Level
Origin
WT (Adult)
WT (Fetal)
Lkb1+/-
Lkb1-/- bud
Lkb1-/- cys
C
Stem/TA cluster
Serrated-specific gene set
Lkb1+/- vs. WT (Adult)
Lkb1-/- bud vs. WT (Adult)
NES
FDR
0.00
0.01
0.02
0.03
0.04
0.05
Enriched in
Lkb1-deficient
Significant
No
Yes
D
Serrated-specific genes (Stem/TA cluster)
UMAP_2
UMAP_1
E
Serrated-specific genes (Stem/TA cluster)
Expression Level
Clusters
Stem cells
WT (Adult)
Lkb1+/-
Lkb1-/- bud
Lkb1-/- cys

## Figure S6

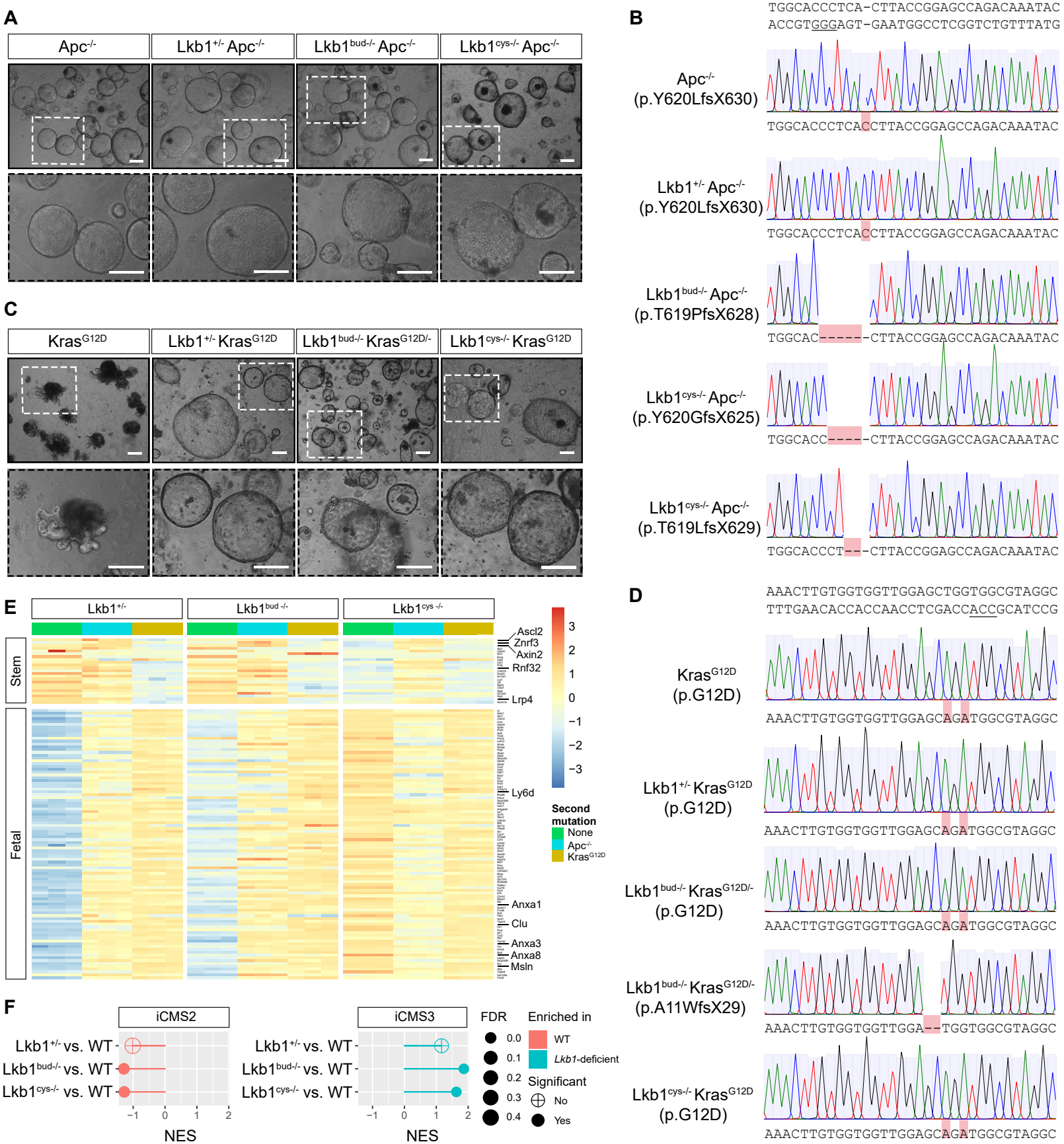
A
Apc-/-
Lkb1+/- Apc-/-
Lkb1bud-/- Apc-/-
Lkb1cys-/- Apc-/-
B
TGGCACCCTCA-CTTACCGGAGCCAGACAAATAC
ACCGTGGGAGT-GAATGGCCTCGGTCTGTTTATG
Apc-/- (p.Y620LfsX630)
TGGCACCCTCACCTTACCGGAGCCAGACAAATAC
Lkb1+/- Apc-/- (p.Y620LfsX630)
TGGCACCCTCACCTTACCGGAGCCAGACAAATAC
Lkb1bud-/- Apc-/- (p.T619PfsX628)
TGGCAC------CTTACCGGAGCCAGACAAATAC
Lkb1cys-/- Apc-/- (p.Y620GfsX625)
TGGCACC-----CTTACCGGAGCCAGACAAATAC
Lkb1cys-/- Apc-/- (p.T619LfsX629)
TGGCACCCT---CTTACCGGAGCCAGACAAATAC
C
KrasG12D
Lkb1+/- KrasG12D
Lkb1bud-/- KrasG12D/-
Lkb1cys-/- KrasG12D
D
AAACTTGTGGTGGTTGGAGCTGGTGGCGTAGGC
TTTGAACACCACCAACCTCGACCACCGCATCCG
KrasG12D (p.G12D)
AAACTTGTGGTGGTTGGAGCAGATGGCGTAGGC
Lkb1+/- KrasG12D (p.G12D)
AAACTTGTGGTGGTTGGAGCAGATGGCGTAGGC
Lkb1bud-/- KrasG12D/- (p.G12D)
AAACTTGTGGTGGTTGGAGCAGATGGCGTAGGC
Lkb1bud-/- KrasG12D/- (p.A11WfsX29)
AAACTTGTGGTGGTTGGA--TGGTGGCGTAGGC
Lkb1cys-/- KrasG12D (p.G12D)
AAACTTGTGGTGGTTGGAGCAGATGGCGTAGGC
E
Lkb1+/-
Lkb1bud -/-
Lkb1cys -/-
Stem
Fetal
Ascl2
Znrf3
Axin2
Rnf32
Lrp4
Ly6d
Anxa1
Clu
Anxa3
Anxa8
Msln
3
2
1
0
−1
−2
−3
Second mutation
None
Apc-/-
KrasG12D
F
iCMS2
iCMS3
Lkb1+/- vs. WT
Lkb1bud-/- vs. WT
Lkb1cys-/- vs. WT
−1
0
1
2
NES
FDR
0.0
0.1
0.2
0.3
0.4
Enriched in
WT
Lkb1-deficient
Significant
No
Yes